PHYSICAL REVIEW B VOLUME 46, NUMBER 8 15 AUGUST 1992-II

# Charge-density-wave pinning and finite-size effects in $NbSe_3$

J. McCarten, D. A. DiCarlo, M. P. Maher, T. L. Adelman, and R. E. Thorne
*Laboratory of Atomic and Solid State Physics, Cornell University, Ithaca, New York 14853*
*and Materials Science Center, Cornell University, Ithaca, New York 14853*
(Received 6 February 1992)

We present a detailed experimental study of the effects of finite crystal size, impurities, and temperature on the properties of charge-density waves (CDW's) in $NbSe_3$. Finite-size effects in $NbSe_3$ are controlled by the crystal thickness $t$. They are large in crystals of ordinary thickness, and remain signficant in high-purity crystals having thicknesses approaching 0.1 mm. In sufficiently thick Ta- and Ti-doped crystals, the threshold electric field $E_T$ for CDW depinning is independent of thickness and varies with the residual resistance ratio $r_R$ as $E_T \propto r_R^{-1.9}$ and $r_R^{-1.4}$, respectively. In thin crystals, $E_T$ increases with decreasing thickness as $E_T = K/t$, where $K$ is roughly proportional to the impurity concentration. $E_T$ is strongly temperature dependent. The fractional increase in $E_T$ as $T \rightarrow 0$ is independent of thickness but decreases rapidly with increasing impurity concentration. The divergence of $E_T$ near $T_{P_2} = 59$ K is described by $E_T \propto (1 - R_H/R_L)^{-0.95}$, where $R_H$ and $R_L$ are the high-field and low-field resistances, respectively. In extremely thin crystals ($t < 0.1$ $\mu$m) near $T_{P_2}$, the sharp threshold vanishes and nonlinear conduction occurs at arbitrarily small fields. Finite-size effects are observed in several other CDW properties. In thin crystals, the crossover frequency $\omega_{co}$ in the ac conductivity varies as $t^{-1}$, the low-frequency dielectric constant $\epsilon(\omega = 1$ MHz) varies as $t$, and the width of the 1/1 Shapiro step varies as $t^{-1}$. Most $NbSe_3$ crystals have irregular cross sections, in which the crystal thickness varies in a series of steps across the crystal width. Such crystals exhibit large $f^{-\alpha}$ noise, complicated coherent oscillation spectra, and complicated mode-locking behavior, when compared with crystals with nearly rectangular cross sections. Analysis of these results indicates that (1) pinning of CDW's in Ta- and Ti-doped $NbSe_3$ is weak; (2) the size dependence of CDW properties is due to a crossover in the dimensionality of the pinning from three to two dimensions which occurs when the crystal thickness becomes smaller than the CDW's bulk transverse phase-phase correlation length; (3) the vanishing of $E_T$ in thin crystals near $T_{P_2}$ is due to thermally assisted depinning of the CDW; and (4) $f^{-\alpha}$-noise and complicated mode-locking behavior are a consequence of CDW velocity shear occurring along steps in crystal thickness. These results have significant implications for the study of nearly every aspect of CDW's in $NbSe_3$.

## I. INTRODUCTION

In quasi-one-dimensional conductors such as $NbSe_3$, interaction between charge-density waves (CDW's) and impurities results in some of the most remarkable transport effects ever discovered.[1] The translational invariance of an incommensurate CDW is destroyed in the presence of impurities (or other crystal defects), so that the CDW tends to be pinned. For applied dc electric fields greater than a threshold field $E_T$, the CDW can depin from the impurities and "slide" through the crystal, resulting in nonlinear dc conduction.[2,3] Pinning gives rise to a radio-frequency resonance in the CDW's small amplitude ($E < 0.1E_T$) ac response.[4] Coherent current oscillations [narrow-band noise (NBN)] observed in response to dc fields[3] and mode-locking phenomena (including Shapiro steps) observed in response to combined ac and dc fields[5] establish that the pinning is periodic in CDW displacements of integral numbers of wavelengths.

In an attempt to develop an understanding of the CDW-impurity interaction, several studies of the effects of intentionally added impurities upon CDW properties, and in particular upon the threshold field $E_T$, have been performed over the last decade.[6–11] The results of these studies have been inconsistent and ambiguous, and have been interpreted using a variety of different models.

More recent work by Borodin *et al.*[12] and by Yetman and Gill[13] showed that $E_T$ also depends upon crystal cross-sectional dimensions. In particular, they found that $E_T$ increases with decreasing crystal cross-sectional area and increasing surface-to-volume ratio.

Here we describe a detailed experimental study of CDW impurity pinning and finite-size effects in $NbSe_3$, which establishes both the character of the pinning and the origin of the size effects. Preliminary results of this study have been published elsewhere.[14–17] An outline of this paper is as follows.

Section II summarizes the basic ideas of the CDW impurity pinning as developed by Fukuyama, Lee, and Rice, with references to Matsukawa's numerical computations to quantify these ideas. Section III reviews previous impurity pinning and finite-size-effect studies. Section IV describes our sample preparation and characterization methods and other experimental details.

Section V contains the bulk of the experimental data. Section V A discusses the effects of finite crystal size on

 ©1992 The American Physical Society

the $T=4.2$ K normal carrier resistivity. Sections V B and V C describe the effects of impurity concentration, crystal size, and temperature on the threshold field $E_T$. Sections V D and V E discuss the size dependencies of the small-signal ac conductivity and of the Shapiro step widths. Narrow-band noise, Shapiro step, and broad-band noise measurements for crystals with uniform and irregular cross sections are compared in Sec. V F.

Section VI presents an analysis of this data. Section VI A discusses the origin of the size dependence of the $T=4.2$ K normal carrier resistivity. Section VI B compares the bulk $E_T$ data with predictions for weak and strong pinning. Section VI C evaluates surface pinning and weak pinning dimensionality crossover interpretations of the finite-size effects. Section VI D discusses the origin of the temperature dependence of $E_T$.

Section VII gives a more general discussion of these results. Section VII A summarizes the successes and failures of weak and strong pinning descriptions for $NbSe_3$. Section VII B compares our results with those of previous studies and suggests reasons for the differences. Section VII C discusses the implications of our results for study of CDW systems. Section VII D speculates on the microscopic nature of the CDW impurity interaction. A short conclusion is presented in Sec. VIII.

## II. CDW-IMPURITY PINNING THEORY

A CDW is a periodic modulation of the conduction electron density $[\rho(\mathbf{r})\sim\rho_0+\rho_1\cos(\mathbf{Q}\cdot\mathbf{r}+\phi)]$ and an associated periodic distortion of the crystal lattice. The CDW state can be described by a complex order parameter $\Psi=\Delta e^{i\phi}$, where $\Delta$ is proportional to the amplitude of the lattice distortion and $\phi$ is the phase (position) of the distortion within the crystal.[18] In the absence of defects, $\Delta$ and $\phi$ are constant. If the CDW wave vector is incommensurate with the underlying lattice periodicity, the CDW's energy will be independent of the absolute value of $\phi$. When an arbitrarily small electric field is applied, the CDW will then slide freely and transport charge (Frohlich conductivity).[19]

Unlike superconductors, the properties of CDW conductors are drastically affected by impurities and other crystal defects. The CDW-impurity interaction energy depends upon the CDW's phase at each impurity site. In the presence of many impurities, the CDW distorts to maximize its energy gain from the impurities while minimizing the cost in strain energy, leading to a spatially varying $\phi(\mathbf{r})$. The CDW thus becomes pinned to the lattice, and its pinning energy is periodic in displacements of the space-averaged phase by $2\pi$. A minimum electric field, the threshold field $E_T$, is required to overcome the pinning force and produce time-averaged CDW motion.

Fukuyama, Lee, and Rice[20–22] (FLR) neglected quantum effects and treated the CDW-impurity interaction within a Ginzburg-Landau framework. They assumed the interaction with a single impurity to be short ranged and well approximated by the form

$$H_{\mathrm{imp}}=v\rho_1\cos[\mathbf{Q}\cdot\mathbf{r}_i-\phi(\mathbf{r}_i)]\ , \tag{1}$$

where $\mathbf{r}_i$ is the impurity site, $\rho_1$ is the CDW charge modulation amplitude, $\mathbf{Q}=2k_F$ is the CDW wave vector, and $v$ is the $\mathbf{Q}$ Fourier component of the potential difference between the impurity and the host atom. In the presence of many randomly distributed impurities, the FLR Hamiltonian for a CDW in $d$ dimensions may be written as[23]

$$H=\int d^d\tilde{r}\,\tilde{f}(\nabla\phi)^2/2+\sum_{i=1}^{N_{\mathrm{imp}}}v\rho_1\cos[\mathbf{Q}\cdot\tilde{\mathbf{r}}_i-\phi(\tilde{\mathbf{r}}_i)]-\int d^d\tilde{r}\,e\tilde{\rho}_{\mathrm{eff}}E\phi/Q\ . \tag{2}$$

Here the transverse dimensions have been rescaled in terms of the strain coefficient anisotropies as $\tilde{x}=\xi_z x/\xi_x$ and $\tilde{y}=\xi_z y/\xi_y$; $\tilde{f}=\xi_x\xi_y f/\xi_z^2$ is the rescaled CDW strain coefficient; $\tilde{\rho}_{\mathrm{eff}}=\xi_x\xi_y\rho_{\mathrm{eff}}/\xi_z^2$ is the rescaled effective charge density coupling the CDW to the electric field; and the electric field $E$ is applied along the quasi-one-dimensional direction $z$. In $T=0$ mean-field theory, $f=\hbar v_F/2\pi A_0$, where $v_F$ is the Fermi velocity along $z$ and $A_0$ is the unit cell cross-sectional area normal to $z$.

FLR showed that the nature of the pinned state is determined by balancing the impurity energy gain associated with optimizing the CDW phase at each impurity site and the elastic energy cost required for phase deformations between impurities.[21,22] They distinguished two types of pinning: (i) strong pinning, in which the CDW phase is pinned at each impurity site; and (ii) weak pinning, in which a phase-coherent domain contains many impurities.

TABLE I. Classical deformable medium model results for weak pinning (Ref. 23).

| | Phase-phase correlation length ($L$) | Threshold electric field ($E_T$) | Pinning energy per phase-coherent domain ($\varepsilon_{\mathrm{dom}}$) |
|---|---|---|---|
| $d=3$ | $\dfrac{45\tilde{f}^2}{(v\rho_1)^2\tilde{n}_i}$ | $\dfrac{Q(v\rho_1)^4\tilde{n}_i^2}{1000e\tilde{\rho}_{\mathrm{eff}}\tilde{f}^3}$ | $\dfrac{300\tilde{f}^3}{(v\rho_1)^2\tilde{n}_i}$ |
| $d=2$ | $\dfrac{6.5\tilde{f}}{(v\rho_1)\tilde{n}_i^{1/2}}$ | $\dfrac{Q(v\rho_1)^2\tilde{n}_i}{20e\tilde{\rho}_{\mathrm{eff}}\tilde{f}}$ | $6.5\tilde{f}$ |
| $d=1$ | $\dfrac{3.5\tilde{f}^{2/3}}{(v\rho_1)^{2/3}\tilde{n}_i^{1/3}}$ | $\dfrac{Q(v\rho_1)^{4/3}\tilde{n}_i^{2/3}}{6e\tilde{\rho}_{\mathrm{eff}}\tilde{f}^{1/3}}$ | $2(v\rho_1)^{2/3}\tilde{f}^{1/3}\tilde{n}_i^{1/3}$ |

Dimensional arguments provide the simplest classification of the weak and strong pinning cases. Following Matsukawa and Takayama,[23] the characteristic CDW elastic energy per impurity $E_E$ is $\tilde{f}\tilde{n}_i^{-1+2/d}$, while the characteristic pinning energy per impurity $E_I$ is just $v\rho_1$. Defining the pinning parameter $\epsilon_i$ as the dimensionless ratio $E_I/E_E$ yields

$$\epsilon_i = v\rho_1/(\tilde{f}\tilde{n}_i^{-1+2/d}) . \tag{3}$$

Thus, if $\epsilon_i \gg 1$, the impurity energy dominates, and the total energy is minimized by fixing the CDW phase at each impurity. In this strong pinning regime, the strain energy can be ignored so that the pinning energy per unit volume $\mathcal{E}_{\text{pin}} = -v\rho_1 n_i$. Balancing this energy with the electric field energy gives a threshold field

$$E_T^{\text{strong}} = v\rho_1 n_i Q / e\rho_{\text{eff}}\phi_T , \tag{4}$$

where $\phi_T$ is the angle through which the CDW must be polarized before depinning.

On the other hand, if $\epsilon_i \ll 1$ the CDW elastic energy dominates. However, from scaling arguments outlined by Imry and Ma,[24] fluctuations in the random impurity pinning potential pin the CDW on a characteristic length scale $L$ (the phase-phase correlation length) if $d<4$. CDW phase variations on a length scale $L$ reduce the impurity energy per rescaled volume ($\mathcal{E}_{\text{imp}}$) by $v\rho_1\tilde{n}_i^{1/2}L^{-d/2}$, but increase the elastic energy per rescaled volume ($\mathcal{E}_{\text{el}}$) by $\kappa d\tilde{f}L^{-2}$, where $\kappa$ is a constant of order unity. Minimizing $\mathcal{E}_{\text{imp}}+\mathcal{E}_{\text{el}}$ with respect to $L$ gives a phase-phase correlation length

$$L = \left[ \frac{4\kappa \tilde{f}}{v\rho_1 \tilde{n}_i^{1/2}} \right]^{2/4-d} , \tag{5}$$

and a threshold field

$$E_T^{\text{weak}} = (4/d - 1)\frac{\kappa d \tilde{f} Q}{L^2 e\tilde{\rho}_{\text{eff}}\phi_T} . \tag{6}$$

Precise values of $\epsilon_i$ for the weak-strong pinning crossover are difficult to estimate analytically. Matsukawa[23] has estimated these values using numerical simulations, in which $\epsilon_i$ was varied and the resulting $E_T$'s compared with the results $E_T \propto \epsilon_i^{4/4-d}$ and $E_T \propto \epsilon_i$ in the weak and strong pinning limits, respectively. For $d=1$ and $d=2$, weak pinning behavior was observed for $\epsilon_i < 10$. For $d=3$, weak pinning behavior was observed for all $\epsilon_i$ values investigated, the greatest of which was 10. Table I summarizes threshold field formulas in 1D, 2D, and 3D weak pinning. The numerical values used for $\kappa$ and $\phi_T$ are consistent with the results of Matsukawa's simulations. Table II compares weak and strong pinning predictions for $E_T$ and $L$.

## III. REVIEW OF PREVIOUS DOPING STUDIES

The most obvious way to study the CDW-impurity interaction is to dope crystals with impurities and study how CDW properties such as $E_T$ vary with impurity concentration and type. Over the past decade a large number of such studies have been reported.[6–11] Most have focused on $NbSe_3$, which undergoes two independent Peierls transitions to CDW states at $T_{P_1}=145$ K and $T_{P_2}=59$ K. Both CDW's are incommensurate along the $b$ direction with a wavelength $\lambda \approx 4b$. A small part of $NbSe_3$'s Fermi surface remains ungapped at low temperatures, so that the residual resistance ratio $r_R = R(300\ \text{K})/R(4.2\ \text{K}) \propto 1/n_i$ can be used to characterize impurity concentrations in individual crystals. The most widely studied dopants have been Ta, which is isoelectronic with Nb and expected to pin weakly, and Ti, a charged impurity expected to pin strongly.

Doping-study results obtained by different researchers have been strikingly inconsistent. Ta-doping studies have found $E_T \propto r_R^{-1}$ (Ref. 9), consistent with strong pinning, and $E_T \propto r_R^{-2}$ (Ref. 6), consistent with weak pinning. For Ta-doped crystals with comparable $r_R$, threshold fields have varied by an order of magnitude. For the undoped crystals used in these studies, $E_T(T=50\ \text{K})$ and $r_R$ have ranged from 60 mV/cm and 10 (Ref. 8), respectively, to 3 mV/cm and 285 (Ref. 11).

CDW pinning by radiation-induced defects has also been investigated.[25] However, the nature and concentrations of the defects formed are hard to characterize, making detailed comparisons with theory difficult.

An important clue as to the nature of CDW pinning has been given by Borodin *et al.*[12] and by Yetman and Gill.[13] They found that in both $o$-$TaS_3$ and $NbSe_3$, the threshold field $E_T$ increases dramatically with decreasing crystal cross-sectional area $A$ and increasing crystal surface-to-volume ratio. Motivated by their results, we decided to systematically examine the impurity concentration and crystal size dependencies of $E_T$ and other CDW properties, in order to clarify both the nature of the pinned state and the origin of the finite-size effects.

## IV. CRYSTAL GROWTH AND CHARACTERIZATION

$NbSe_3$ was chosen for this study for four reasons. (1) It shows most of the effects associated with CDW transport

TABLE II. Comparison: Strong vs 3D weak pinning.

| | Phase-phase correlation length ($L$) | Threshold electric field ($E_T$) | Pinning energy per phase coherent domain ($\varepsilon_{\text{dom}}$) |
|---|---|---|---|
| weak | $\frac{45\tilde{f}^2}{(v\rho_1)^2\tilde{n}_i}$ | $\frac{Q(v\rho_1)^4\tilde{n}_i^2}{1000e\tilde{\rho}_{\text{eff}}\tilde{f}^3}$ | $\frac{90\tilde{f}^3}{(v\rho_1)^2\tilde{n}_i}$ |
| strong | $\sim n_i^{-1/3}$ | $\frac{Q(v\rho_1)n_i}{e\rho_{\text{eff}}}$ | $v\rho_1$ |

more cleanly than other materials. (2) Part of its Fermi surface remains ungapped at low temperatures so that the $r_R$ can be used to characterize impurity concentrations. (3) The crystal size dependence of $E_T$ is large. (4) It has been used in most previous doping studies, facilitating comparisons.

$NbSe_3$ crystals grow as long, ribbonlike whiskers with typical lengths (along the $b$ direction) of several millimeters to several centimeters, widths (along $c$) of 1–1000 $\mu$m, and thicknesses (along $a^*$) of 0.1–20 $\mu$m. The $NbSe_3$ crystals studied here were prepared by vapor transport using the methods described in Ref. 26. As discussed in Ref. 26, careful crystal growth procedures are crucial in performing meaningful studies of the effects of impurities. In previous doping studies, chemical analysis results were not reported. Instead, it was assumed that the impurity types and concentrations in the transported crystals were the same as those in the starting materials. This is a poor assumption. Doping by impurities not derived from the starting materials can be significant. More importantly, oxygen present in the starting materials efficiently getters Ta, Ti, and other impurities, so that dopant concentrations in the crystals are usually smaller than those in the starting materials. The growth procedures in Ref. 26 provided reasonably reproducible background impurity levels in undoped crystals, and reasonable control over Ta and Ti concentrations in doped crystals. Ta- and Ti-doping levels in the most heavily doped crystals were determined using techniques including atomic emission spectroscopy, atomic absorption spectroscopy, proton-induced x-ray emission, and ICP-mass spectrometry.

In order to characterize the finite-size effects, the crystal length $l$ and width $w$ were measured using an optical microscope. The crystal thickness $t$ was then calculated from these dimensions and the measured room-temperature resistance $R$ using $t=l/(\sigma w R)$, where $\sigma$ is the room-temperature conductivity. Previously reported values[27] of $\sigma$ vary between $1.6\times10^3$ and $10\times10^3$ $\Omega^{-1}\,\mathrm{cm}^{-1}$. We used a value of $\sigma=5.4\times10^3$ $\Omega^{-1}\,\mathrm{cm}^{-1}$, which was determined using the method described in Appendix A. Since $NbSe_3$ crystals typically have irregular cross-sectional shapes (in which the crystal thickness changes in a series of steps across the crystal width), the measured width is the maximum width, and the calculated thickness is the average thickness.

Experimentally, we find that the crystal thickness controls the finite-size effects in $NbSe_3$; width variations in crystals of ordinary dimensions have little effect. There are two reasons for this. First, typical crystal thicknesses are an order of magnitude or more smaller than typical crystal widths. Second, CDW correlation lengths are longer along $a^*$ than along $c$.[28,29] Consequently, all data for finite-size effects presented in the following sections are expressed as a function of thickness.

The transport measurements reported here were made using either a nitrogen-helium dipstick (for $T=77$ K and $T=4.2$ K data) or using a closed-cycle helium refrigerator with a helium exchange gas. Unless otherwise noted, all measurements were performed in a four-probe configuration with contacts formed using silver or gold paste.

## V. DATA AND RESULTS

### A. Impurity concentration and size dependence of the residual resistance ratio

Measurements of the residual resistance ratio $r_R=R(T=300\text{ K})/R(T=4.2\text{ K})$ have been widely used[6–11,14,15] to characterize impurity concentrations in $NbSe_3$. Assuming that $R(T=300\text{ K})$ is independent of impurity concentration and that defect scattering determines $R(T=4.2\text{ K})$, the $r_R$ should be related to the concentration of intentionally added impurities $n_i$ by

$$r_R^{-1}=r_{R_0}^{-1}+b_i^{-1}n_i\ , \tag{7}$$

where $r_{R_0}$ is the contribution from residual defects and $b_i$ depends upon impurity type.

However, as shown in Fig. 1 for crystals from a single undoped $NbSe_3$ growth, the $r_R$ also depends upon crystal thickness: It decreases with decreasing thickness in thin crystals ($t<2$ $\mu$m) and is approximately thickness independent in thick crystals. Similar behavior is observed in doped crystals, where the thickness for the bulk to finite-size crossover decreases with increasing doping level. From chemical-analysis results for heavily doped crystals and the measured bulk (i.e., thick crystal) $r_R$ values, we estimate

$$b_{\mathrm{Ta}}\approx3\times10^{20}\ \mathrm{cm}^{-3} \tag{8}$$

and

$$b_{\mathrm{Ti}}\approx1\times10^{19}\ \mathrm{cm}^{-3}\ . \tag{9}$$

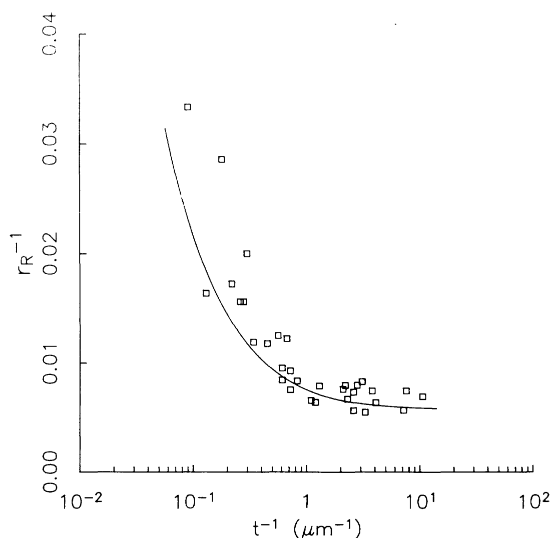


FIG. 1. $r_R^{-1}$ vs crystal thickness $t$ for undoped $NbSe_3$ crystals with $r_R\approx220$. The solid line is a fit by Fuch's theory of surface scattering, assuming 100% diffuse surface scattering and a transverse single-particle mean-free path of 0.7 $\mu$m.

The uncertainty is roughly a factor of 2 in the latter value and somewhat smaller in the former value.

Large scatter in $r_R$ values for crystals from a given growth has been noted previously, but was attributed to crystal-to-crystal variations in impurity concentrations. This scatter is primarily (if not entirely) a finite-size effect. Unless this size dependence is explicitly accounted for, impurity concentrations should only be characterized using the $r_R$ of thick crystals. The $r_R$ values quoted for $NbSe_3$ growths in subsequent sections are average values measured for thick crystals.

### B. Impurity concentration and size dependence of the threshold field

#### 1. *Ta doping*

Figure 2 shows the threshold field $E_T(T=77\text{ K})$ versus inverse crystal thickness $t^{-1}$ for an undoped growth and for three growths with different Ta concentrations. For all four growths, $E_T$ is approximately thickness independent for large thicknesses and varies approximately as $t^{-1}$ for small thicknesses. The characteristic thickness $t_c$ for the crossover to size-independent behavior decreases with increasing impurity concentration. In addition, the size-related increase in $E_T$ as $t \to 0$, $\Delta E_T(t) = E_T(t) - E_T^{\text{bulk}}$, increases with increasing impurity concentration. For example, for the $r_R=35$ growth, $\Delta E_T(0.2\ \mu\text{m}) \approx 2200$ mV/cm, while for the $r_R=220$ growth, $\Delta E_T(0.2\ \mu\text{m}) \approx 800$ mV/cm.

For our initial studies,[14] a measurement temperature of $T=77$ K was chosen to simplify characterization of a large number of samples. However, most previous doping studies focused on the temperature where $E_T$ is a minimum, since the onset of CDW conduction at threshold is sharpest at this temperature.[6,9] Figure 3 shows $E_T$ versus $t^{-1}$ for the $T_{P_1}$ CDW at 120 K and the $T_{P_2}$ CDW at 50 K, for crystals from an undoped growth with $r_R=220$ and from a Ta-doped growth with $r_R=35$. The overall behavior is similar to that in Fig. 2: $E_T$ is size independent in thick crystals and increases with decreasing thickness in thin crystals. Size effects are larger for the $T_{P_2}$ CDW: For the undoped growth, $E_T$ for the $T_{P_2}$ CDW is still significantly $t$ dependent at thicknesses of $\sim 20\ \mu$m, while $E_T$ for the $T_{P_1}$ CDW has saturated to its bulk value. As summarized in Table III, for both CDW's the size-related increase in $E_T$ as $t \to 0$ increases with in-

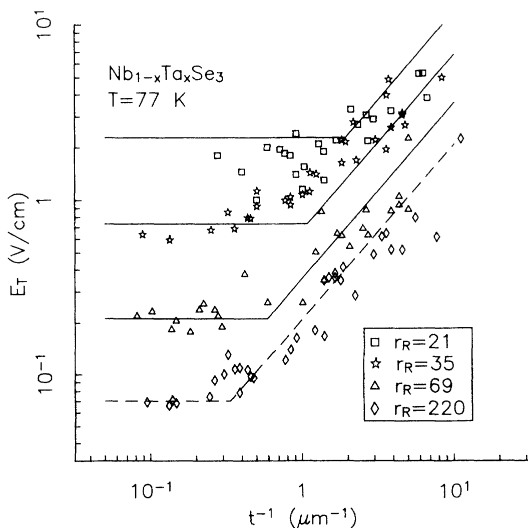


FIG. 2. Threshold electric field $E_T$ at 77 K vs inverse thickness $t^{-1}$ for Ta-doped $NbSe_3$. The solid lines represent the 3D and 2D weak pinning fits of Eqs. (10) and (21), as discussed in Sec. VI C 2.

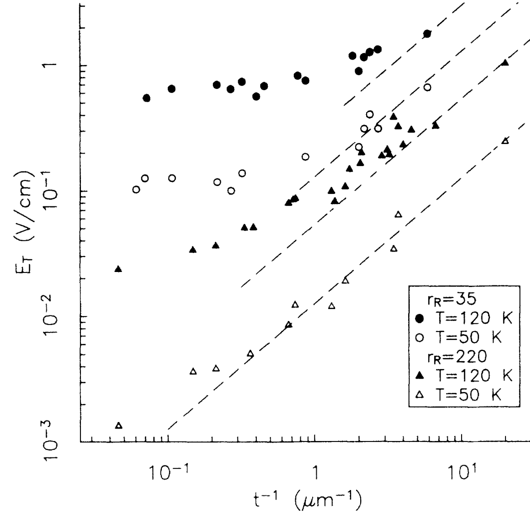


FIG. 3. Threshold electric field $E_T$ for the $T_{P_1}$ CDW at 120 K and the $T_{P_2}$ CDW at 50 K vs $t^{-1}$ in undoped ($r_R=220$) and moderately Ta-doped ($r_R=35$) $NbSe_3$. At $T=120$ K, the crossover from bulk to size-dependent behavior occurs at thicknesses of approximately 5 and 2 $\mu$m in the $r_R=220$ and $r_R=35$ crystals, respectively. At $T=50$ K, the crossover occurs at $t \approx 5\ \mu$m in the $r_R=35$ crystals, but no crossover is evident for $t$ up to 20 $\mu$m in the $r_R=220$ crystals. The solid lines indicate approximate thin-crystal asymptotes $E_T \propto t^{-1}$.

TABLE III. (a) $\Delta E_T(t) \equiv E_T(t) - E_T^{\text{bulk}}$ vs $r_R$ for $Nb_{1-x}Ta_xSe_3$. (b) Comparison of $\Delta E_T(t)$ at $T=77$ K for Ta- and Ti-doped $NbSe_3$.

| | | (a) | | | |
|---|---|---|---|---|---|
| | $T_{P_1}$ CDW $T=120$ K | | | $T_{P_2}$ CDW $T=50$ K | |
| $r_R$ | $E_T^{\text{bulk}}$ (V/cm) | $\Delta E_T(0.2\ \mu\text{m})$ (V/cm) | $r_R$ | $E_T^{\text{bulk}}$ (V/cm) | $\Delta E_T(0.2\ \mu\text{m})$ (V/cm) |
| 220 | 0.025 | 0.35 | 220 | 0.002 | 0.08 |
| 35 | 0.65 | 1.1 | 35 | 0.13 | 0.5 |
| | | (b) $T=77$ K | | | |
| | $Nb_{1-x}Ta_xSe_3$ | | | $Nb_{1-x}Ti_xSe_3$ | |
| 69 | 0.2 | 1.0 | 53 | 0.15 | 1.1 |
| 35 | 0.8 | 2.2 | 27 | 0.35 | 1.7 |
| 21 | 2.0 | 4.0 | 8 | 2.0 | 6.0 |

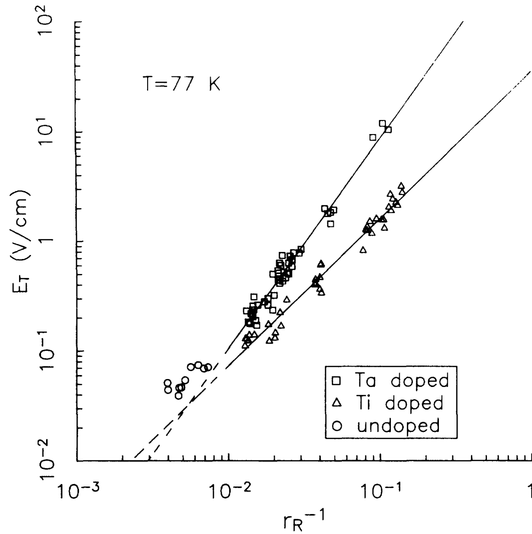


FIG. 4. Comparison of $E_T$-$r_R^{-1}$ data for thick Ta- and Ti-doped $NbSe_3$ crystals. The solid lines represent least-squares fits of the form $E_T = A(r_R^{-1})^b$ with $b = 1.9$ for the Ta-doped crystals and $b = 1.35$ for the Ti-doped crystals. Undoped crystals were excluded from the fits.

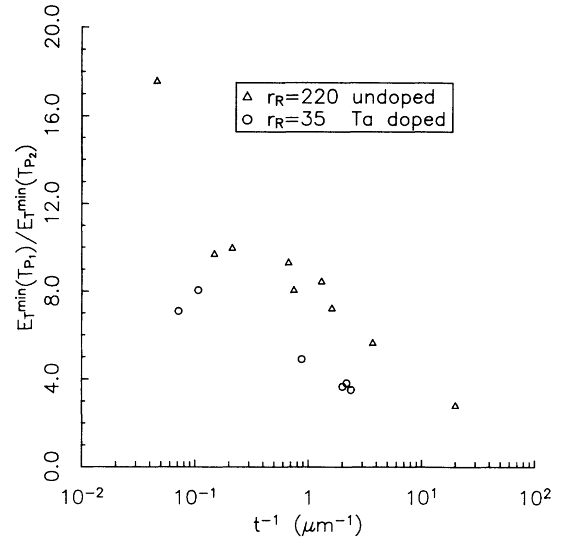


FIG. 6. Ratio of the minimum thresholds for the $T_{P_1}$ and $T_{P_2}$ CDW's, $E_T^{min}(T_{P_1})/E_T^{min}(T_{P_2})$, vs $t^{-1}$ for undoped and Ta-doped $NbSe_3$ crystals.

creasing impurity concentration.

In order to characterize the bulk pinning behavior of a given impurity, only thick crystals for which $E_T$ is thickness independent should be examined. Figure 4 shows $E_T(T=77\text{ K})$ versus $r_R^{-1}$ for thick crystals (i.e., $t \gg t_c$) from four Ta-doped growths and two undoped growths. The large scatter typical of such plots[9] is eliminated by exclusion of crystals from the finite-size regime. A least-squares fit to the data for Ta-doped crystals of the form

$$E_T = A(r_R^{-1})^b \tag{10}$$

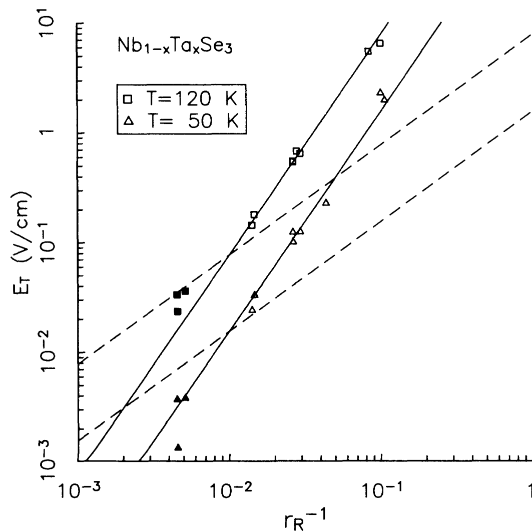


FIG. 5. Threshold electric field $E_T$ at 120 and 50 K vs $r_R^{-1}$ for thick Ta-doped $NbSe_3$ crystals. The solid and dashed lines correspond to the weak pinning ($E_T \propto r_R^{-2}$) and strong pinning ($E_T \propto r_R^{-1}$) predictions, respectively.

yields $A = 750 \pm 90$ V/cm and $b = 1.9 \pm 0.1$. The exponent $b$ very close to FLR's square-law prediction for weak pinning.

Figure 5 shows $E_T$ versus $r_R^{-1}$ for the $T_{P_1}$ CDW at $T = 120$ K and the $T_{P_2}$ CDW at $T = 50$ K, for thick undoped and Ta-doped crystals. A least-squares fit of Eq. (10) to the Ta-doped growths gives $A = 630 \pm 90$ V/cm and $b = 1.94 \pm 0.05$ at $T = 120$ K, and $A = 280 \pm 80$ V/cm and $b = 2.17 \pm 0.09$ at 50 K. The agreement with FLR's weak pinning prediction is again very good. Unlike the $T = 77$ K data in Fig. 4, at $T = 120$ K and 50 K the data for the undoped crystals fall close to the extrapolated fits to the Ta-doped crystals. This difference arises from the effects of impurities on the temperature dependence of $E_T$, as will be discussed in Sec. V C.

Figure 6 shows the ratio of the minimum $E_T$'s for the two CDW's, $E_T^{min}(T_{P_1})/E_T^{min}(T_{P_2})$, versus $t^{-1}$ for the data of Fig. 3. For thick crystals, this ratio is $\sim 8$ for $r_R = 35$ and $\sim 20$ for the undoped material. For thin crystals, this ratio decreases to $\sim 3$.

### 2. *Ti doping*

Figure 7 shows $E_T(T=77\text{ K})$ versus $t^{-1}$ for five Ti-doped growths. Unlike Ta, which is isoelectronic with Nb, Ti is expected to form a charged and thus more strongly pinning defect. A previous study[7] found $E_T \propto r_R^{-1}$, consistent with FLR's strong pinning prediction. The qualitative behavior in Fig. 7 is the same as for Ta-doped crystals in Fig. 2: $E_T$ is approximately thickness independent in thick crystals, $E_T \propto t^{-1}$ in thin crystals, the characteristic thickness for the bulk to finite-size crossover $t_c$ decreases with increasing impurity concentration, and the size-related increase in $E_T$ in thin crys-

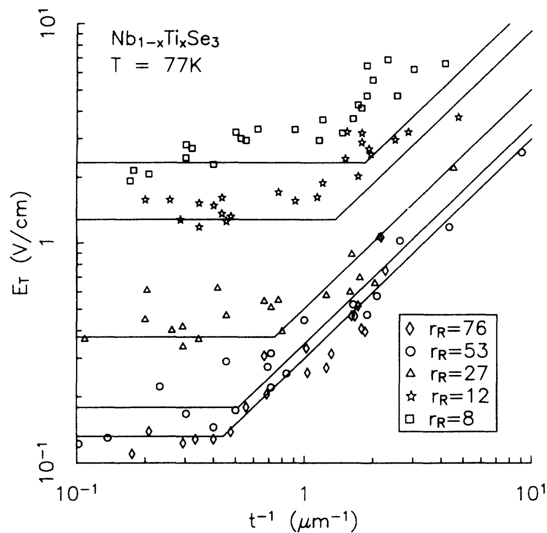


FIG. 7. Threshold electric field $E_T$ at 77 K vs inverse thickness $t^{-1}$ for Ti-doped $NbSe_3$. The solid lines represent the 3D and 2D weak pinning fits of Eqs. (10) and (21), as discussed in Sec. VI C 2.

tals $\Delta E_T(t)$ increases with increasing Ti concentration. In addition, for Ta- and Ti-doped growths with similar bulk $E_T$ values, $t_c$ and $\Delta E_T(t)$ are approximately the same.

Figure 4 shows $E_T$ versus $r_R^{-1}$ for thick crystals (i.e., $t \gg t_c$) from five Ti-doped growths. A least-squares fit of Eq. (10) to the data for the Ti-doped crystals yields $A = 30 \pm 5$ V/cm and $b = 1.35 \pm 0.1$. The power-law exponent thus falls between FLR's weak and strong pinning predictions. Measurements of the minimum threshold fields for thick Ti-doped crystals yield $E_T^{\min}(T_{P_1})/E_T^{\min}(T_{P_2}) \approx 8$, just as for Ta-doped crystals.

Figure 4 indicates that for crystals with $r_R \approx 10$, $E_T$ for Ta-doped crystals is approximately five times larger than for Ti-doped crystals. However, from Eqs. (7), (8), and (9), Ti has a much larger effect on the $r_R$ than Ta. Consequently, $E_T$'s for a given Ti concentration are much larger than for an equal Ta concentration, consistent with the expectation that Ti should pin the CDW more strongly.

Summarizing the results of our Ta- and Ti-doping studies, we observe the following.

(1) $E_T \propto r_R^{-2}$ and $E_T \propto r_R^{-1.35}$ in thick Ta- and Ti-doped crystals, respectively.

(2) In the finite-size regime, $E_T \sim K/t$, where the constant of proportionality $K$ increases with increasing impurity concentration.

(3) The characteristic thickness $t_c$ for the crossover from bulk to size-dependent behavior decreases with increasing impurity concentration.

(4) The ratio $E_T^{\min}(T_{P_1})/E_T^{\min}(T_{P_2})$ increases with increasing thickness, and saturates to approximately 8-in-thick Ta- and Ti-doped crystals.

### C. Temperature dependence of the threshold field

Many CDW properties vary strongly with temperature, both near $T_P$ where the order parameter $\Delta$ varies strongly, and at low temperatures where $\Delta \approx \Delta(T=0)$. As noted by Fleming,[30] $E_T$ in undoped $NbSe_3$ exhibits a minimum near $T \sim 0.8T_P$, and increases sharply as $T_P$ is approached from below and somewhat more gradually as $T \to 0$. The effects of impurity concentration on this temperature dependence have been studied previously, but the results obtained have been inconsistent. One study found that doping strongly suppressed $E_T$'s low-temperature increase,[6] while another found little effect.[31] Neither study accounted for finite-size effects. We thus have measured $E_T(T)$ as a function of both impurity concentration and crystal thickness, to determine if size effects are the cause of previous inconsistencies, and to evaluate possible origins of the temperature dependence.

#### 1. Increase in $E_T$ as $T \to 0$

Figures 8 and 9 show $E_T$ versus temperature for $NbSe_3$ crystals with thicknesses between 0.05 μm and 20 μm, taken from a single undoped growth. For both the $T_{P_1}$ and $T_{P_2}$ CDW's, the temperature $T_{\min}$ at which $E_T$ is a minimum increases with decreasing thickness. However, the fractional increase in $E_T(T)$ for $T < T_{\min}$ is approximately independent of crystal thickness. Data for $T < T_{\min}$ have previously been fit[32] using the form $E_T \propto e^{-T/T_0'}$. Fits of this form to the data of Figs. 8 and 9 yield $T_0'$ values which vary little with crystal thickness.[33]

Figures 10 and 11 compare $E_T(T)$ for crystals of similar thickness but containing different Ta concentrations. The fractional increase in $E_T$ as $T \to 0$ decreases and the

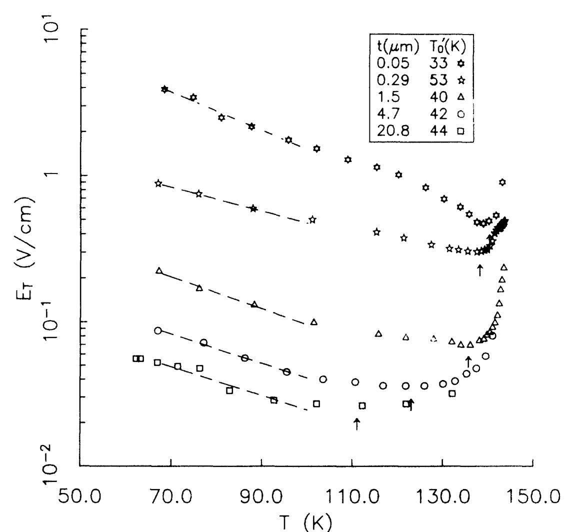


FIG. 8. Threshold electric field $E_T$ vs temperature for the $T_{P_1}$ CDW in undoped $NbSe_3$ crystals of different thicknesses. The data for $T < 100$ K are fit by $E_T \propto \exp(-T/T_0')$ (dashed lines). The arrows indicate where $E_T$ is a minimum.

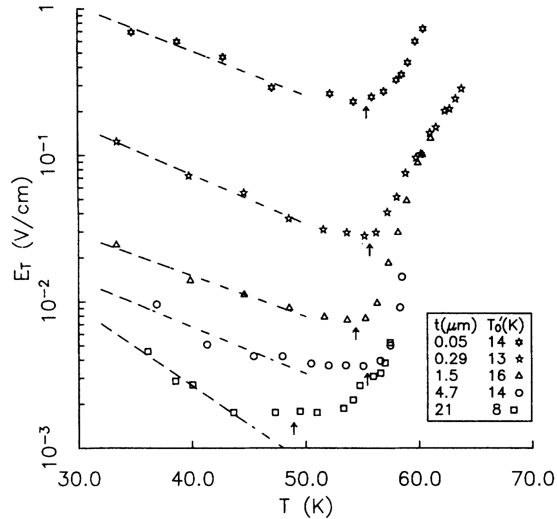


FIG. 9. Threshold electric field $E_T$ vs temperature for the $T_{P_2}$ CDW in undoped $NbSe_3$ crystals of different thicknesses. The data for $T < 48$ K is fit by $E_T \propto \exp(-T/T_0')$ (dashed lines). The arrows indicate where $E_T$ is a minimum.

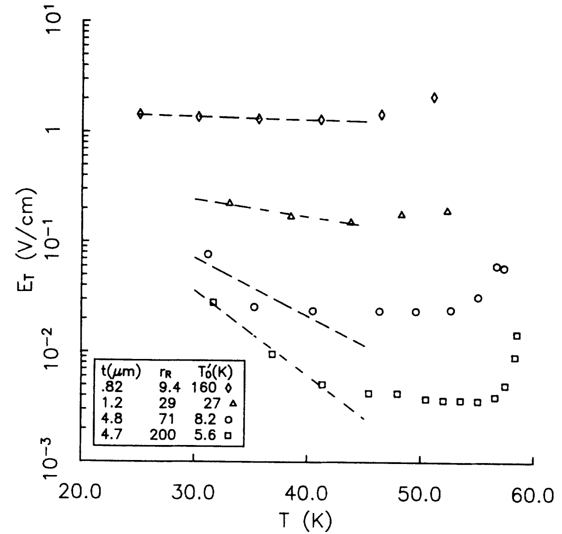


FIG. 11. Threshold electric field $E_T$ for the $T_{P_2}$ CDW vs temperature for crystals containing different Ta concentrations. Dashed lines indicate the fit $E_T \propto \exp(-T/T_0')$.

characteristic temperature $T_0'$ increases with increasing Ta concentration.

### 2. *Divergence of $E_T$ as $T \to T_P$*

Divergences near phase transitions are generally analyzed in terms of a reduced temperature. This is difficult in $NbSe_3$ because the Peierls transition temperature is somewhat ill defined. Figure 12 shows the low-field resistivity $\rho$ and $(1/\rho)(d\rho/dT)$ versus temperature near $T_{P_2}$ for an undoped crystal with $A = 7.9\ \mu m^2$ and $t = 1.4\ \mu m$. $T_P$ is frequently determined as the temperature where $(1/\rho)(d\rho/dT)$ is a maximum,[34,35] which is 57.5 K for this crystal. However, $\rho$ is a local minimum at 59.0 K, and nonlinear conduction due to the $T_{P_2}$ CDW is observed at temperatures up to 61.0 K. It is not obvious which of these three temperatures is closest to the "true" transition temperature.

The definition of $T_P$ is further complicated because as the crystal thickness decreases, the resistive transition becomes more gradual[36] and the highest temperature at which nonlinear conduction can be measured increases. This is illustrated in Fig. 13. For the thinner crystal, nonlinear conduction from the $T_{P_2}$ CDW is observed up to 61 K, while for the thicker crystal, nonlinear conduc-

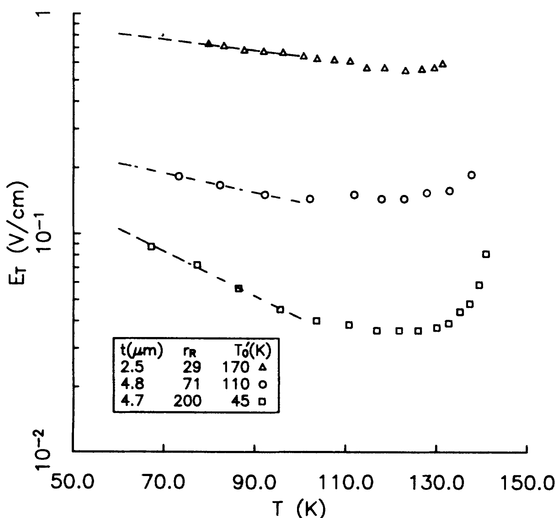


FIG. 10. Threshold electric field $E_T$ for the $T_{P_1}$ CDW vs temperature for crystals containing different Ta concentrations. Dashed lines indicate the fit $E_T \propto \exp(-T/T_0')$.

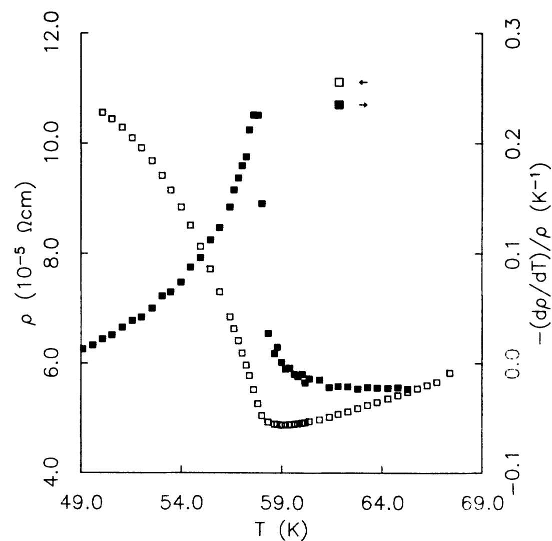


FIG. 12. Low-field resistivity $\rho$ and $-(d\rho/dT)/\rho$ vs temperature near the $T_{P_2}$ transition for an undoped $NbSe_3$ crystal with $t = 1.4\ \mu m$ and $A = 7.9\ \mu m^2$. For this crystal, the temperatures at which $\rho$ is a local minimum (59 K) and $-(d\rho/dT)/\rho$ is a local maximum (57.5 K) differ by 1.5 K.

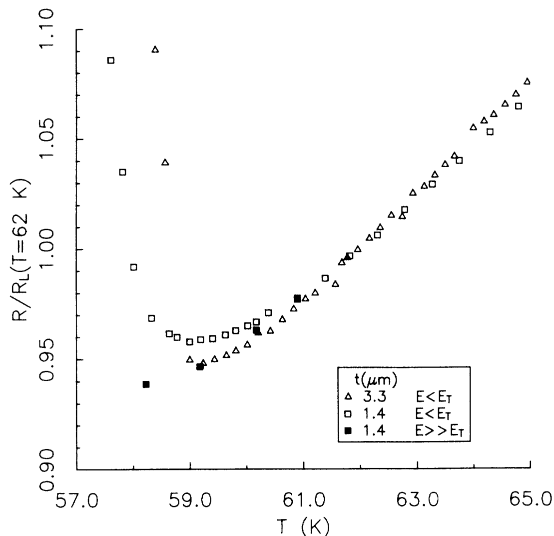


FIG. 13. Resistance vs temperature for two crystals of different cross-sectional dimensions. The high-field resistance was determined at a field below the depinning field of the $T_{P_1}$ CDW.

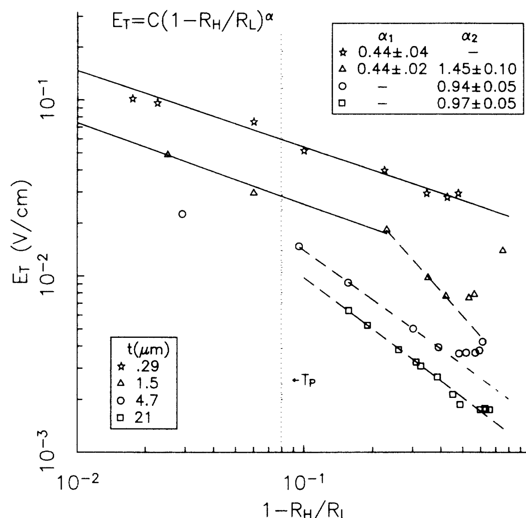


FIG. 15. Threshold field $E_T$ vs $1-R_H/R_L$ near the $T_{P_2}$ CDW transition for undoped $NbSe_3$ crystals with different thicknesses. For thick crystals, $E_T \propto (1-R_H/R_L)^{0.95}$, and for the thinnest crystal, $E_T \propto (1-R_H/R_L)^{0.45}$. The vertical line indicates where $-(d\rho/dT)/\rho$ is a maximum for the $t=0.29$ $\mu$m crystal.

tion is not observed above 59 K (Ref. 37). We have observed similar behavior in all crystals examined to date. Anomalous nonlinear conduction above the temperature of the resistance minimum has been observed previously,[35] but its dependence on crystal size was not noted. Maki[38] has attributed this nonlinear conduction to depinning of pretransitional fluctuations which reduce the normal carrier viscosity, and has suggested that the magnitude of the effect should depend upon dimensionality.

To avoid the problem of defining $T_P$, we instead analyze the divergence of $E_T$ in terms of the CDW condensate density $\rho_{\text{eff}}$, which goes to zero at the transition. The

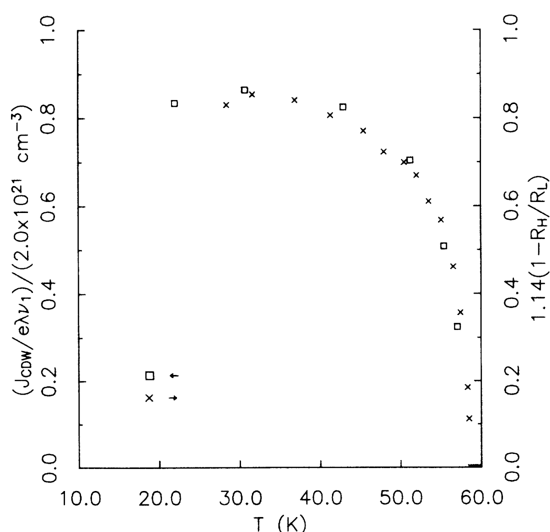


FIG. 14. Effective CDW condensate density $\rho_{\text{eff}}$ vs temperature for the $T_{P_2}$ CDW, as deduced from narrow-band noise measurements (squares) and from the ratio of the high- and low-field resistances (triangles).

condensate density can be determined in two ways: (i) using $\rho_{\text{eff}}=J_{\text{CDW}}/e\lambda\nu_1$, where $J_{\text{CDW}}$ is the nonlinear current density and $\nu_1$ is the narrow-band noise fundamental frequency; and (ii) using $\rho_{\text{eff}} \propto (1-R_H/R_L)$,[39] where $R_H$ and $R_L$ are the low- and high-field resistances and where it is assumed that the high-field CDW mobility $\mu_H^{\text{CDW}}$ equals the low-field normal carrier mobility $\mu_L^N$. Figure 14 shows $\rho_{\text{eff}}$ as determined by these two methods versus temperature for the $T_{P_2}$ CDW.[40] The first method cannot be used very near $T_P$ because the NBN becomes too small to measure. Over the temperature range where both methods can be used, the temperature dependencies are in good agreement.

Figure 15 shows $E_T$ of the $T_{P_2}$ CDW versus $1-R_H/R_L$ for four undoped crystals of various thicknesses. Here $E_T$ is defined as the electric field required for the low-field differential resistance to drop by 0.25%. Two types of power-law behavior are evident. In the two thickest crystals, $E_T \propto (1-R_H/R_L)^{-\alpha}$, where $\alpha=0.95\pm0.05$. In the thinnest crystal ($t=0.29$ $\mu$m), $\alpha=0.45\pm0.05$. For the 1.5-$\mu$m-thick crystal, a crossover between the two types of behavior is observed.

### 3. *Threshold rounding in thin crystals near $T_P$*

In very thin crystals near $T_P$, the form of the nonlinear *I-V* characteristic changes qualitatively. Figure 16 shows the differential resistance versus electric field for the $T_{P_2}$ CDW at $T=56$ K, for three undoped crystals with thicknesses of 4.7, 0.29, and 0.05 $\mu$m. The sharp conduction threshold observed in the thickest crystal is absent in the thinnest crystal, for which nonlinear conduction appears to occur at arbitrarily small fields.

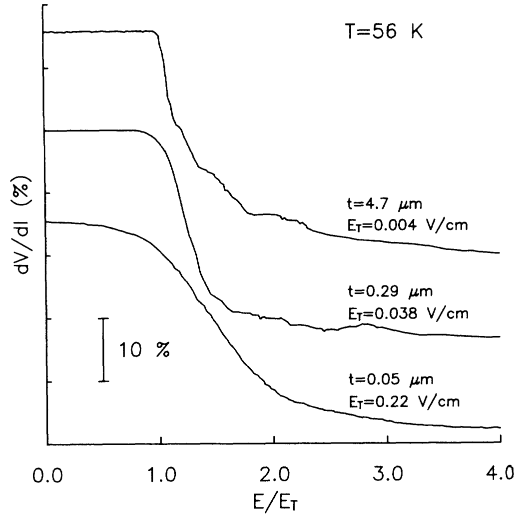


FIG. 16. Differential resistance $dV/dI$ vs $E/E_T$ at 56 K for undoped $NbSe_3$ crystals with different thicknesses. $E_T$ for the $t=0.05$ $\mu$m crystal is ill defined and was estimated by scaling its $dV/dI$ curve with those of thicker crystals.

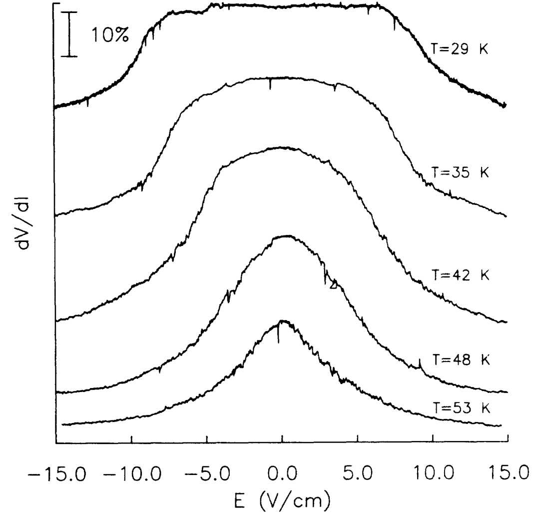


FIG. 18. Differential resistance $dV/dI$ vs $E$ at five temperatures below $T_{P_2}$ for an extremely small crystal having a length, width, and thickness of 38, 0.5, and 0.026 $\mu$m, respectively.

Figure 17 shows the differential resistance versus electric field for the $t=0.05$ $\mu$m crystal at several temperatures. Threshold rounding is evident even in the $T=50$ K data, where the CDW order parameter is near its $T=0$ value, although the rounding appears to decrease with decreasing temperature. Figure 18 shows $dV/dI$ versus $E$, measured in a two-probe configuration, for an extremely thin crystal with $t=0.025$ $\mu$m, $A=0.013$ $\mu m^2$, and $l=38$ $\mu$m. For $T>35$ K, the onset of nonlinear conduction clearly occurs at arbitrarily small fields and only for temperatures below 35 K is it even possible to define $E_T$. More pronounced rounding in even thinner crystals has been independently observed by Gill and Zaitsev-Zotov[41] for both the $T_{P_1}$ and $T_{P_2}$ CDW's in $NbSe_3$.

This rounding may be important in interpreting the re-

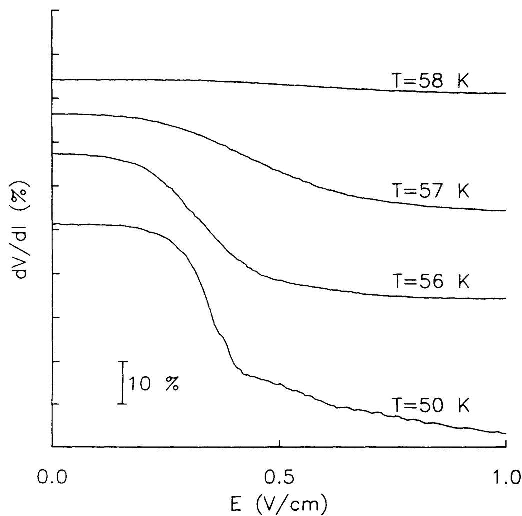


FIG. 17. Differential resistance $dV/dI$ vs $E$ for the $t=0.05$ $\mu$m crystal of Fig. 16 at four temperatures below $T_{P_2}$.

sults of the previous section for the threshold divergence near $T_P$. In particular, the exponent $\alpha \approx 0.45$ we obtained for the $t=0.29$ and 0.05 $\mu$m crystals in Fig. 15 may be an artifact of our definition of $E_T$. As $T \rightarrow T_P$, the onset of CDW conduction in these crystals becomes more rounded and the CDW current to normal current ratio decreases, making the conduction onset more difficult to resolve. Consequently, $E_T$ and the exponent $\alpha$ become ill defined.

Summarizing our results for the temperature dependence of $E_T$ in $NbSe_3$, we find the following.

(1) The temperature $T_{\min}$, where $E_T$ is a minimum, increases with decreasing thickness.

(2) $T_{\min}$ decreases with increasing $n_{Ta}$.

(3) The characteristic temperature $T_0'$ for the low-temperature increase in $E_T$ shows no significant thickness dependence.

(4) $T_0'$ increases with increasing $n_{Ta}$.

(5) Near $T_P$ in thick ($t>2$ $\mu$m) undoped crystals, $E_T \propto (1-R_H/R_L)^{-0.95}$.

(6) Anomalous depinning above $T_P$ is observed in thin crystals.

(7) The onset of CDW conduction at threshold becomes increasingly rounded with increasing temperature and decreasing crystal thickness.

### D. Size dependence of the small-signal ac conductivity

Another manifestation of CDW pinning is a strong frequency dependence at rf frequencies of the small-signal ac conductivity $\sigma_{CDW}(\omega)$. For small CDW displacements, the local pinning force is expected to be harmonic, so that the ac response should have the general form of a damped harmonic oscillator. ac conductivity measurements have often been analyzed using a single-coordinate model,[42] for which $\sigma_{CDW}(\omega)$ has the form[43]

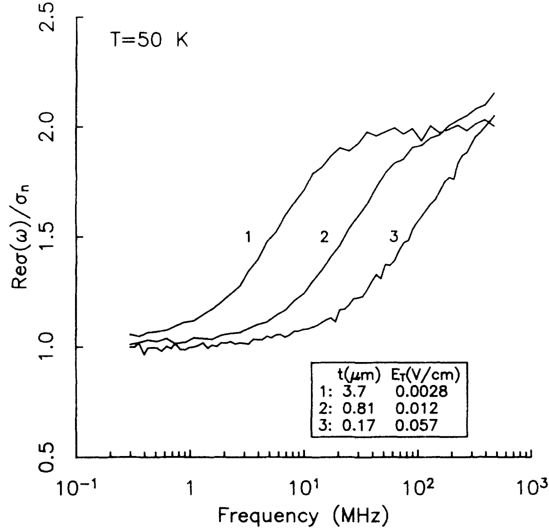


FIG. 19. Real part of the small-signal ac conductivity at $T=50$ K for undoped $NbSe_3$ crystals of different thicknesses.

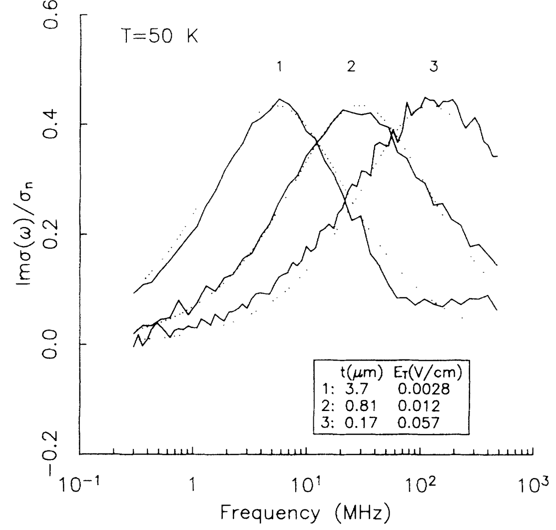


FIG. 20. Imaginary part of the small-signal ac conductivity at $T=50$ K for undoped $NbSe_3$ crystals of different thicknesses. The fits (dashed lines) are discussed in Appendix B.

$$\mathrm{Re}\sigma_{\mathrm{CDW}}(\omega)=\frac{\rho_{\mathrm{eff}}e^2}{\gamma m^*}\frac{\omega^2}{\omega^2+\omega_{\mathrm{co}}^2} \tag{11a}$$

and

$$\mathrm{Im}\sigma_{\mathrm{CDW}}(\omega)=\frac{\rho_{\mathrm{eff}}e^2}{\gamma m^*}\frac{\omega\omega_{\mathrm{co}}}{\omega^2+\omega_{\mathrm{co}}^2} . \tag{11b}$$

Here $\gamma$ is the CDW damping coefficient, $m^*$ is the CDW effective mass, $\rho_{\mathrm{eff}}$ is the CDW condensate density, and

$$\omega_{\mathrm{co}}=\frac{e\rho_{\mathrm{eff}}QE_T}{\gamma m^*} \tag{12}$$

is the crossover frequency. $\mathrm{Im}\sigma_{\mathrm{CDW}}(\omega)$ has a maximum at $\omega=\omega_{\mathrm{co}}$ and a full width at half maximum of $2\sqrt{3}\omega_{\mathrm{co}}$. Previous experiments[44] on doped $TaS_3$ found that $\omega_{\mathrm{co}}$ increases with increasing impurity concentration and scales with $E_T$ as predicted by Eq. (12). Fits to the data can be improved by assuming a distribution of $\omega_{\mathrm{co}}$ values, to reflect the distribution of local pinning strengths within a crystal.[45]

Because $\sigma_{\mathrm{CDW}}(\omega)$ contains information about the distribution of pinning strengths which is not contained within $E_T$, we have investigated its size dependence. $NbSe_3$ crystals were attached to a 50-Ω-strip line using gold paint,[46] and the ac conductivity measured using a Hewlett Packard 8753A network analyzer. The measurements were performed on the $T_{P_2}$ CDW because the size effects are larger, the ac response occurs at lower frequencies, and shunting of the ac response by normal carriers is much smaller for this CDW than for the $T_{P_1}$ CDW.

Figures 19 and 20 show $\mathrm{Re}\sigma_{\mathrm{CDW}}(\omega)$ and $\mathrm{Im}\sigma_{\mathrm{CDW}}(\omega)$ versus frequency at $T=50$ K for three undoped crystals of various thickness. The CDW response shifts to higher frequencies with decreasing thickness. The crossover frequency $\omega_{\mathrm{co}}$ and the half-width of $\mathrm{Im}\sigma_{\mathrm{CDW}}(\omega)$ both vary inversely with thickness, indicating that the shift is homogeneous. This suggests that the increase in CDW pinning strength with decreasing thickness is uniform within the crystal cross section. The fits in Fig. 20 are discussed in Appendix B and assume a Lorentzian distribution of $\omega_{\mathrm{co}}$ values.

Table IV summarizes results for these three samples and two others, including values for the low-frequency dielectric constant $[\mathrm{Re}\epsilon_{\mathrm{CDW}}(\omega)=1-4\pi\,\mathrm{Im}\sigma_{\mathrm{CDW}}(\omega)/\omega]$ evaluated at 1 MHz.[47] The dielectric constant decreases with increasing thickness, but since $E_T$ increases the product $\mathrm{Re}\epsilon(\omega=1\text{ MHz})E_T$ is roughly constant. This product is predicted to satisfy the relation[44] $\epsilon(\omega=0)E_T=ke/A_0$, where $k$ is a constant of order unity which depends upon the details of the pinning. We find

TABLE IV. ac conductivity crossover frequency $f_{\mathrm{co}}$, dielectric constant $\epsilon$(1 MHz) (Ref. 47), and $E_T$ vs thickness for the $T_{P_2}$ CDW at $T=50$ K in undoped $NbSe_3$.

| $l$ (mm) | $A$ ($\mu m^2$) | $t$ ($\mu$m) | $f_{\mathrm{co}}$ (MHz) | $\epsilon/\epsilon_0$ | $E_T$ (V/cm) | $\epsilon E_T A_0/e$ |
|---|---|---|---|---|---|---|
| 3.15 | 115 | 3.7 | 5.7±1 | $4.9\times10^9$ | 0.0028 | 0.7 |
| 0.95 | 4.8 | 0.81 | 17.5±4 | $1.1\times10^9$ | 0.012 | 0.7 |
| 1.33 | 0.98 | 0.54 | 12±4 | $2.4\times10^9$ | 0.013 | 1.6 |
| 0.38 | 0.47 | 0.37 | 60±10 | $8.0\times10^8$ | 0.035 | 1.4 |
| 0.55 | 0.35 | 0.17 | 140±40 | $5.6\times10^8$ | 0.057 | 1.6 |

$k \approx 1$, consistent with values obtained previously[44] for Nb-doped $TaS_3$.

### E. Size dependence of CDW mode locking

Shapiro steps provide one of the more spectacular manifestations of CDW interaction with impurities.[5,48–51] As first noted by Monceau, Richard, and Renard,[48] when a voltage $V(t)=V_{dc}+V_{ac}\cos(2\pi\nu_{ac}t)$ is applied to a CDW crystal, the dc $I$-$V$ characteristic exhibits "steps" where the dc CDW current remains constant while the dc voltage varies. These steps are due to mode locking of the internal CDW frequency $\nu_1$ (i.e., the narrow-band noise frequency) associated with dc current flow with the applied ac frequency $\nu_{ac}$. When $\nu_n$ is near a rational multiple of $\nu_{ac}$, periodic CDW interaction with impurities results in an additional time-averaged pinning force which adds to the applied dc electric force. This time-averaged pinning force adjusts so as to adjust the dc CDW current until $\nu_n = p\nu_{ac}/q$, where $p$ and $q$ are integers.[50] The step width $\delta V$ is proportional to the maximum of this time-averaged pinning force, and thus provides information about the CDW-impurity interaction in a dynamic limit.

We have studied the crystal thickness dependence of the 1/1 mode-locked step width. Four-probe measurements were made on undoped $NbSe_3$ crystals near $T=120$ K, where the quality of the mode locking is highest. Only high-quality crystals for which the mode locking was complete (i.e., for which the differential resistance on the 1/1 step rose to its $E<E_T$ value) or nearly complete[52] were used. The step width was calculated as

$$\delta V = R_L \int \frac{dV/dI - R_H}{R_L - R_H} dI \ , \tag{13}$$

where the integral is over the mode-locked region, $R_L$ is the $E<E_T$ resistance, and $R_H$ is the differential resistance just outside the mode-locked region.

The mode-locked step widths exhibit Bessel-like oscillations as a function of ac amplitude.[50,51] Figure 21 shows the first (and largest) step width maximum normalized by the $V_{ac}=0$ threshold voltage, $\delta V_{1/1}^{max}/V_T$, versus $t^{-1}$ for an applied ac frequency of 20 MHz. Parameters for all of the crystals shown are summarized in Table V. Although crystal thicknesses vary by a factor of 40 and $E_T$'s vary by a factor of 10, the ratio $\delta V_{1/1}^{max}/V_T$ is approximately constant. This suggests that the pinning mechanism responsible for the size dependence of $E_T$ is also responsible for the time-averaged pinning force which produces mode locking in the sliding state.

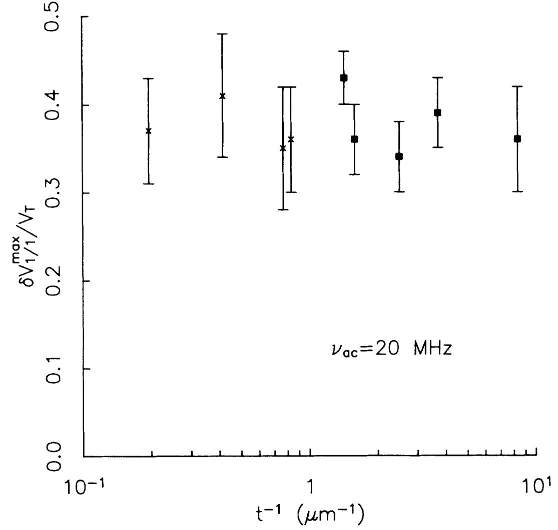


FIG. 21. 1/1 mode-locked step width maximum for $\nu_{ac}=20$ MHz normalized by the $V_{ac}=0$ dc threshold voltage, $\delta V_{1/1}^{max}/V_T$, vs $t^{-1}$ at $T=120$ K for undoped $NbSe_3$. The squares (■) and crosses (×) represent samples for which the mode locking was complete or nearly complete, respectively.

### F. Effects of nonuniform crystal thickness

For most $NbSe_3$ crystals, the crystal cross section remains constant in size and shape over lengths of at least several millimeters, much longer than the sample lengths used in transport measurements. However, for essentially all crystals, the cross-section shape is highly irregular. The crystal thickness changes in a series of steps running along the whisker axis, with step heights that can be comparable to the average thickness. Since CDW properties depend upon thickness, these thickness variations might be expected to have important consequences. For example, since $E_T$ depends upon crystal thickness, the thicker parts of the crystal might be expected to depin at lower

TABLE V. 1/1 mode-locked step width for $\nu_{ac}=20$ and 40 MHz vs crystal thickness for the $T_{P_1}$ CDW in undoped $NbSe_3$ ($r_R=220$) at 120 K. Mode locking of the 1/1 step was complete for the first five samples ($t \le 0.70$ $\mu$m) and nearly complete (Ref. 52) for the other samples.

| $l$ (mm) | $A$ ($\mu m^2$) | $t$ ($\mu$m) | $\delta V_{1/1}^{max}/V_T$(20 MHz) | $\delta V_{1/1}^{max}/V_T$(40 MHz) | $E_T$ (V/cm) |
|---|---|---|---|---|---|
| 0.35 | 0.23 | 0.12 | 0.36±0.06 | | 0.64 |
| 0.31 | 0.49 | 0.27 | 0.39±0.04 | 0.47±0.04 | 0.23 |
| 0.65 | 0.40 | 0.40 | 0.34±0.04 | 0.43±0.04 | 0.33 |
| 0.88 | 1.2 | 0.63 | 0.36±0.04 | 0.43±0.06 | 0.21 |
| 0.83 | 0.52 | 0.70 | 0.43±0.03 | 0.50±0.04 | 0.19 |
| 0.75 | 8.8 | 1.2 | 0.36±0.06 | 0.39±0.06 | 0.095 |
| 0.88 | 12.3 | 1.3 | 0.35±0.07 | 0.40±0.07 | 0.090 |
| 1.28 | 33 | 2.4 | 0.41±0.07 | 0.44±0.08 | 0.11 |
| 1.18 | 49 | 5.1 | 0.37±0.06 | | 0.060 |

fields than the thinner parts, with velocity shear occurring along the boundaries between them.

To investigate the effects of thickness steps, we performed a very simple experiment. An undoped $NbSe_3$ crystal having one large thickness step (as illustrated in the inset of Fig. 22) was selected and cut in half lengthwise (i.e., the cut was made perpendicular to the whisker axis). One of these halves was then carefully cleaved along the step. This procedure yielded one crystal with an irregular cross section (referred to as the whole) and two crystals with more nearly rectangular cross sections (referred to as parts 1 and 2). Electrical contacts were applied far from the cut ends to avoid any damaged regions. Measurements of the narrow-band noise, mode locking, and broad-band noise were made on several samples prepared in this way. All measurements were performed near $T=120$ K, where the NBN and mode-locking quality are highest. Data presented here are for two representative samples whose parts had the following lengths, maximum widths, and average thicknesses: Sample $A$, 0.96 mm$\times$4.4 $\mu$m$\times$0.95 $\mu$m for part 1, 1.2 mm$\times$3.4 $\mu$m$\times$1.12 $\mu$m for part 2, and 0.9 mm$\times$7.8 $\mu$m$\times$1.0 $\mu$m for the whole; sample $B$, 0.7 mm$\times$33 $\mu$m$\times$1.5 $\mu$m for part 1, 0.8 mm$\times$25 $\mu$m$\times$2.2 $\mu$m for part 2, and 1.4 mm$\times$57 $\mu$m$\times$2.0 $\mu$m for the whole.

Figure 22 shows the fundamental NBN spectral peaks for part 1, whose cross section was nearly rectangular, and for the whole of sample $A$. The whole's fundamental is very broad and shows substantial structure. Part 1's fundamental consists of only one extremely sharp peak ($Q\approx350$) and a second much smaller peak at lower frequency. In samples with large thickness differences between parts 1 and 2, the peaks in the whole can be unambiguously identified as coming from parts 1 and 2; the thicker part gives a higher frequency peak than the thinner part. Since the NBN frequency $\nu_n$ is proportional to the CDW velocity, this implies that the CDW moves with different time-averaged velocities in different parts of the whole's cross section. Velocity shear must then occur along the thickness step.

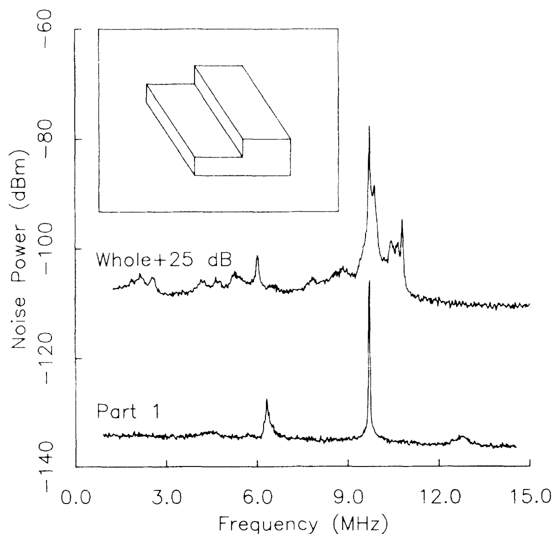


FIG. 22. Narrow-band noise fundamental spectral peaks for the whole and for part 1 of sample $A$ (discussed in the text). The spectral width in part 1, which had a nearly rectangular cross section, is much smaller. The inset schematically illustrates the crystal studied, whose cross section had one large step in its thickness running parallel to the whisker axis. The crystal was split along the step to produce parts 1 and 2.

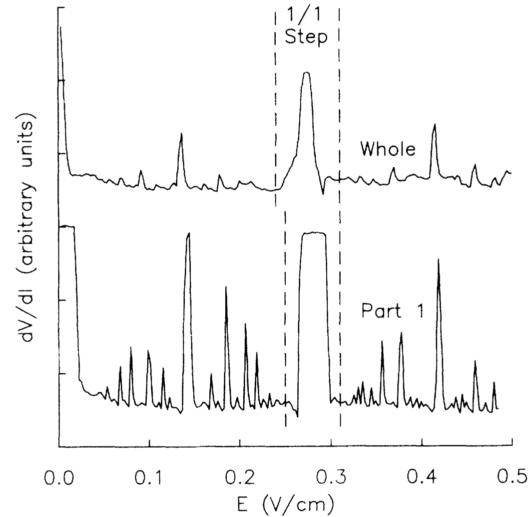


FIG. 23. Differential resistance $dV/dI$ vs dc bias for sample $A$, measured in the presence of a 10-MHz ac field. The ac amplitude was chosen to obtain the maximum mode-locked width of the 1/1 peak. The completeness of the mode locking correlates with the uniformity of the crystal cross section.

Figure 23 shows the differential resistance $dV/dI$ of sample $A$ measured in the presence of a 10-MHz ac voltage. Mode locking of the whole's 1/1 peak is only 65% complete, and few subharmonic peaks are visible. In contrast, the 1/2 and 1/1 peaks of part 1 lock completely, and subharmonics down to $p/q=1/7$ can be resolved. This difference in mode locking quality is a consequence of the difference in CDW velocity distributions between the whole and part $A$, as reflected in the NBN spectra of Fig. 22.

CDW conductors exhibit enormous $f^{-\alpha}$ or broad-band noise (BBN). Previous studies[53–55] found that $\alpha\approx0.4-0.8$, and that the BBN amplitude scaled with sample volume, suggesting a bulk origin. Figure 24 shows the normalized broad-band noise power per unit volume versus frequency for sample $B$. The NBN fundamental frequency for the whole and for each of the parts was set at 50 MHz to ensure that the CDW current densities were comparable and that no NBN peaks were inside the BBN measurement window. The BBN per unit volume in the whole is more than two orders of magnitude greater than in either of the two parts. Similar behavior was observed in sample $A$. This clearly identifies the thickness discontinuity as being primarily responsible for the difference in BBN amplitudes.

These results are consistent with those of Thorne *et al.*[50] For a crystal with a nearly perfect rectangular

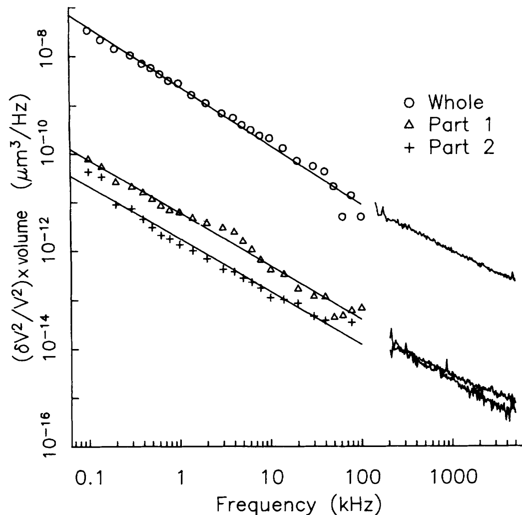


FIG. 24. Normalized broad-band noise power per unit volume vs frequency for sample $B$. The more than two orders-of-magnitude difference between the whole and parts 1 and 2 is due to the thickness step in the whole's cross section. Data below and above 100 kHz were obtained using a lock-in amplifier and spectrum analyzer, respectively.

cross section, they observed a NBN fundamental peak with $Q \approx 30\,000$ at a frequency $\nu_n \approx 84$ MHz, nearly 150 subharmonic mode-locked peaks between threshold and the 1/1 step, and almost no BBN except at dc biases very near threshold. In our own measurements on a large number of samples over the last three years, we have consistently observed a strong correlation between cross-section uniformity and mode-locking quality.

The origin of the thickness steps is unclear, but they may arise from small-angle grain boundaries. To check whether the effects discussed above are a consequence of thickness-dependent pinning or of disruption of the crystal lattice along the steps, we have cleaved crystals along both the $b$-$c$ and $b$-$a$ crystallographic planes. The results obtained were qualitatively similar in both cases, suggesting that thickness-dependent pinning is responsible.

An interesting effect was observed when a crystal with one large thickness step was cycled twice between room temperature and 125 K. On the first cooldown, only one rather gradual depinning was observed at a threshold field of 23 mV/cm. On the second cooldown, two distinct depinnings were observed at threshold fields of 32 mV/cm and 61 mV/cm. These thresholds were almost identical to those measured for two nearly rectangular parts obtained by cleaving the original crystal along the $b$-$c$ plane; all three thresholds scaled with the maximum thickness of the whole and its parts. Variations in $E_T$ and other CDW properties with temperature cycling have been noted previously. Cycling-induced cracking along thickness steps provides a simple explanation for these observations.[56]

Summarizing the results of this section, we find that (1) the CDW shears easily when inhomogeneously pinned; (2) coherent CDW response occurs only in samples with rectangular cross sections; (3) multiple NBN peaks and incomplete mode locking in undoped crystals result from irregular crystal cross sections; (4) CDW shear occurring along thickness steps provides the primary source of BBN in $NbSe_3$ at $T \approx 125$ K.

## VI. ANALYSIS

### A. Size dependence of the $r_R$

Normal carrier scattering by crystal surfaces provides the simplest explanation for the $r_R$ versus thickness data of Fig. 1. This scattering should lead to an increase in $R(4.2\text{ K})$ and thus a decrease in $r_R$ with decreasing crystal thickness. Fuchs's theory of surface scattering[57,58] predicts that the conductivities of films of finite and infinite thickness should have the ratio

$$\frac{\sigma(t)}{\sigma_\infty} = 1 - \frac{3}{2\kappa}\int_0^1 du \frac{(u-u^3)(1-p)[1-\exp(-\kappa/u)]}{1-p\exp(-\kappa/u)}, \tag{14}$$

where $\kappa = t/l$, $l$ is the low-temperature bulk mean-free path, and $p$ is the specularity parameter. $p=0$ corresponds to purely diffuse scattering, while $p=1$ corresponds to purely specular scattering. Typical experimental values of $p$ for metal films vary from 0 to 0.9, depending upon the metal and upon how the film is prepared.[59] The solid line in Fig. 1 is a fit of Eq. 14 assuming $p=0$ and a transverse mean-free path $l_{a^*} = 0.7\ \mu$m.[60] Fits with $p$ values of up to 0.8 also give reasonable fits; for $p=0.8$, $l_{a^*} \approx 10\ \mu$m. Neither $p$ nor $l_{a^*}$ can be accurately determined because of the scatter in the data.

These $a^*$ mean-free paths are roughly consistent with the results of magnetotransport measurements by Ong.[61] For a $NbSe_3$ crystal with $r_R = 60$, Ong deduced $T = 4.2$ K normal carrier mobilities of $3\times10^5$ and $2\times10^4$ cm²/Vs along the **b** and **c** directions, respectively. Assuming a Fermi velocity $v_F = 2.5\times10^7$ cm/s and a carrier mass $m = m_e$, these mobilities correspond to mean-free paths of $l_b \approx 35\ \mu$m and $l_c \approx 2.5\ \mu$m. Comparable values are expected along $a^*$. Mean free paths in the $r_R = 220$ crystals of Fig. 1 should be roughly four times larger.

An alternative explanation for the thickness dependence of the $r_R$ is that the low temperature resistance is determined by normal carrier scattering off the CDW. As will be discussed in Sec. VI C, the CDW phase-phase correlation length is predicted to decrease with decreasing thickness, so that enhanced CDW normal carrier interaction might be expected in thin crystals. History-dependent changes in the normal carrier resistance of a few percent suggest that this interaction is important; whether it is large enough to account for the observed size dependence is unclear.

### B. Impurity concentration dependence of $E_T$: bulk pinning

#### 1. Ta doping

Characterizing the nature of the CDW impurity interaction is complicated because of finite-size effects, and

TABLE VI. Microscopic parameters for the two CDW's in $NbSe_3$.

| | $T_{P_1}=144$ K | $T_{P_2}=59$ K | References |
|---|---|---|---|
| $\lambda$ | 14.3 Å | 13.2 Å | 107, 108 |
| $Q$ (along $b^*$) | 0.439 Å$^{-1}$ | 0.475 Å$^{-1}$ | 107, 108 |
| $\rho_c$ $(T=0)$ | $1.9\times10^{21}$ cm$^{-3}$ | $2.05\times10^{21}$ cm$^{-3}$ | 109 |
| $A_0$ | 73.6 Å$^2$ | 73.6 Å$^2$ | 110 |
| $v_F$ | $2.5\times10^7$ cm/s | $2.7\times10^7$ cm/s | 111 |
| $\Delta(T=0)$ (mean field) | 0.022 eV | 0.0089 eV | 1 |
| $\Delta(T\to0)$ (tunneling) | 0.090 eV | 0.037 eV | 103 |
| $f$ | 0.0035 eV Å$^{-1}$ | 0.0038 eV Å$^{-1}$ | 20 |
| $\xi_{b^*}:\xi_{a^*}:\xi_{c^*}$ | $1:\frac{1}{9}:\frac{1}{25}$ | $1:\frac{1}{9}:\frac{1}{25}$ | 112 |
| $\xi_{b^*}=\hbar v_F/\pi\Delta$ | 25 Å | 60 Å | 22 |

because pinning by residual defects determines the measured properties of undoped and lightly doped crystals. Size effects are easily accounted for by using only thick crystals. As shown in Figs. 4 and 5 and discussed in Sec. V B 1, bulk $E_T$ data for both the $T_{P_1}$ and $T_{P_2}$ CDW's in Ta-doped $NbSe_3$ are well described by $E_T \propto r_R^{-2}$, consistent with FLR's prediction for 3D weak pinning.

Neglecting for the moment the effects of pinning by residual defects, the Ta pinning strength $(v\rho_1)_{Ta}$ can be calculated from the 3D weak pinning formula for $E_T$ given in Table I using values determined from weak pinning fits of Eq. (10), the $n_i$-$r_R$ relation of Eq. (8), and the appropriate microscopic parameters for $NbSe_3$ given in Table VI. This calculation yields Ta pinning strengths $(v\rho_1)_{Ta}$ of 4.3 and 4.5 meV for the $T_{P_1}$ CDW at 120 and 77 K, respectively, and 3.0 meV for the $T_{P_2}$ CDW at 50 K.[62] These values can in turn be used to calculate the pinning parameter $\epsilon_i$. Substituting appropriate values from Table VI into Eq. (3) yields

$$\epsilon_i \approx 200 v\rho_1 (n_i/1\times10^{19}\ \text{cm}^{-3})^{1/3} \tag{15}$$

for both CDW's, where $v\rho_1$ is given in eV. The values of $(v\rho_1)_{Ta}$ calculated above then give $\epsilon_i \approx 1$ for heavily Ta-doped crystals with $r_R \approx 10$ (and smaller values for more lightly doped crystals). This value is well within Matsukawa's calculated range for weak pinning.[23] Consequently, a weak pinning analysis provides a self-consistent account of $E_T$-$r_R^{-1}$ data in thick Ta-doped $NbSe_3$ crystals.

The same cannot be said of a strong pinning analysis. The $E_T$-$r_R^{-1}$ data of Figs. 4 and 5 clearly do not fit the strong pinning prediction $E_T \propto r_R^{-1}$ (indicated by the dashed line in Fig. 5). Using $E_T=9.5$ V/cm and $r_R=10$ for heavily Ta-doped crystals together with appropriate values from Table VI, the strong pinning threshold-field formula [Eq. (4)] yields $(v\rho_1)_{Ta}=1.5\times10^{-5}$ eV. Substituting this value into Eq. (15) then gives $\epsilon_i=4\times10^{-3}$, at least three orders of magnitude into the weak-pinning limit. This inconsistency is far too large to be accounted for by uncertainties in our parameters. The strong-pinning analysis thus fails dramatically.

*2. Ti doping*

Analysis of CDW pinning in Ti-doped crystals is more complicated. As shown in Fig. 4, $E_T$-$r_R^{-1}$ data for thick Ti-doped crystals are well described by Eq. (10) with a power-law exponent $b=1.35$, in between FLR's predictions for weak and strong pinning.

Pinning by defects other than Ti can account for this exponent. Residual defects determine the properties of undoped crystals. If, relative to the residual defects, the dopant impurities have a larger effect on the $r_R$ than on $E_T$, then small dopant concentrations will produce larger fractional changes in the $r_R$ than in $E_T$. Fits to $E_T$-$r_R^{-1}$ data will then yield smaller exponents than if the pinning were due to the dopants alone.

The effects of pinning by more than one impurity type on $E_T$-$r_R^{-1}$ relations can be quantified as follows. If both the dopant impurities and the residual impurities pin the CDW weakly, then the impurity fluctuation energy is modified from $v\rho_1 n_i^{1/2}$ for a single impurity to $[\sum(v\rho_1)_j^2 n_j]^{1/2}$ for $j$ different impurities. For two impurity types, the arguments of Sec. II yield for the 3D case

$$E_T=E_{T_0}+2\sqrt{E_{T_0}}a_w n_i + a_w^2 n_i^2 , \tag{16}$$

where $E_{T_0}$ is the threshold field due to residual impurities, $n_i$ is the dopant impurity concentration, and $a_w$ determines $E_T$ in the absence of residual pinning, as in Table I. If both impurity types pin strongly, the pinning energies add and

$$E_T=E_{T_0}+a_s n_i . \tag{17}$$

This expression is expected to be approximately valid in the case of weak residual pinning for small dopant concentrations. Substituting for $n_i$ using Eq. (7) yields

$$\sqrt{E_T}=\sqrt{E_0^w}+a_w b_i r_R^{-1} \tag{18}$$

for weak pinning and

$$E_T=E_0^s+a_s b_i r_R^{-1} \tag{19}$$

for strong pinning, where $\sqrt{E_0^w}=\sqrt{E_{T_0}}-a_w b_i r_{R_0}^{-1}$, $E_0^s=E_{T_0}-a_s b_i r_{R_0}^{-1}$, and $r_{R_0}$ is the $r_R$ due to residual impurities. If $E_0 \ll E_{T_0}$, then FLR's weak and strong pin-

ning power laws are recovered. If this relation does not hold, then smaller power-law exponents (i.e., less than 2 for weak pinning and less than 1 for strong pinning) are predicted. Consequently, the exponent of 1.35 observed for Ti-doped $NbSe_3$ suggests that Ti acts as a weak pinning impurity.

Figure 25 shows $\sqrt{E_T}$ versus $r_R^{-1}$ for thick Ta- and Ti-doped crystals. The solid lines represent the fits of Eq. (18), made with the constraint that the fits pass through the point $(E_{T_0}, r_{R_0}^{-1})$ measured for undoped crystals.[63] Both fits are excellent, consistent with weak pinning by both Ta and Ti. From the $a_w$ value deduced from the Ti fit, $(v\rho_1)_{Ti} \approx 0.011$ eV, roughly 2.5 times larger than for Ta. For heavily Ti-doped crystals with $n_i \approx 100$ ppm, $r_R = 10$, and $E_T = 1.6$ V/cm, Eq. (15) thus yields a pinning parameter $\epsilon_i \approx 0.9$, well into the weak-pinning regime. If Ti is instead assumed to pin strongly, then Eqs. (4) and (15) yield $(v\rho_1)_{Ti} \approx 5\times10^{-5}$ eV and $\epsilon_i \approx 5\times10^{-3}$. As with Ta, the strong pinning assumption fails dramatically.

Table VII compares $E_T$ values for Ta- and Ti-doped crystals. As discussed in Sec. V B 2, $E_T$'s for comparable $r_R$'s are larger for Ta than for Ti. However, $E_T$'s for comparable impurity concentrations are much larger for Ti than for Ta. Direct comparisons at equal concentrations are difficult,[64] but for $n_i \approx 100$ ppm, bulk thresholds for Ti-doped crystals are roughly 40 times larger than would be measured in crystals comparably doped with Ta. This threshold ratio is consistent with a pinning strength ratio of only 2.5 since in 3D weak pinning, $E_T \propto (v\rho_1)^4$.

If Ta and Ti both pin the CDW weakly, then why do power-law fits to $E_T$-$r_R^{-1}$ data for Ta and Ti-doped $NbSe_3$ yield such different exponents? This difference arises from the difference in their $E_0$ values, given by the $y$ intercepts in Fig. 25. For Ti, $E_0 \approx 0.40 E_{T_0}$, whereas for Ta, $E_0 \approx 0.01 E_{T_0}$. $E_0$ is larger for Ti because Ti affects the

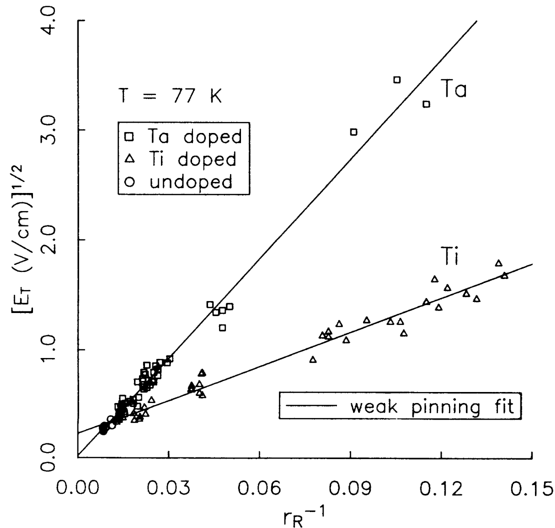


FIG. 25. Comparison of $E_T$-$r_R^{-1}$ data for thick Ta- and Ti-doped $NbSe_3$ crystals at $T = 77$ K. The solid lines represent the weak pinning fits provided by Eq. (18).

TABLE VII. $E_T$ ($T = 77$ K) and $r_R$ vs impurity concentration for Ta- and Ti-doped $NbSe_3$.

| Ta | | | Ti | | |
|---|---|---|---|---|---|
| $n_i$ (ppm) | $r_R$ | $E_T$ (V/cm) | $n_i$ (ppm) | $r_R$ | $E_T$ (V/cm) |
| $\approx 100$ | 200 | 0.050 | 20 | 35 | 0.15 |
| 500 | 50 | 0.60 | 40 | 20 | 0.55 |
| 2600 | 10 | 10 | 100 | 8 | 2.0 |

$r_R$ much more than $E_T$, i.e., $b_i/a_w$ is much larger for Ti than for Ta. Appendix C calculates the exponent that would be obtained from a power-law fit of Eq. (10) to Eq. (18) over the range $E_{T_0} < E_T < E_T^{max}$, assuming $E_0 = 0.40 E_{T_0}$. This exponent is plotted as a function of $E_T^{max}$ in Fig. 26. Even for $E_T^{max} = 1000 E_{T_0}$ (much larger than could be measured experimentally) the exponent is only 1.6. A similar plot for $E_0 = 0.01 E_{T_0}$ shows that an exponent of 1.9 is recovered for an $E_T^{max}$ of only $E_{T_0}$, comparable to the range of our Ta data in Fig. 4.

### C. Size dependence of CDW properties

#### 1. *Surface pinning interpretation*

Early experiments on the crystal size dependence of $E_T$ were interpreted as evidence that the CDW is more strongly pinned near crystal surfaces than in the bulk.[13,65] A variety of mechanisms could give rise to enhanced CDW pinning near surfaces. For example, surface defects or surface impurities might interact strongly with

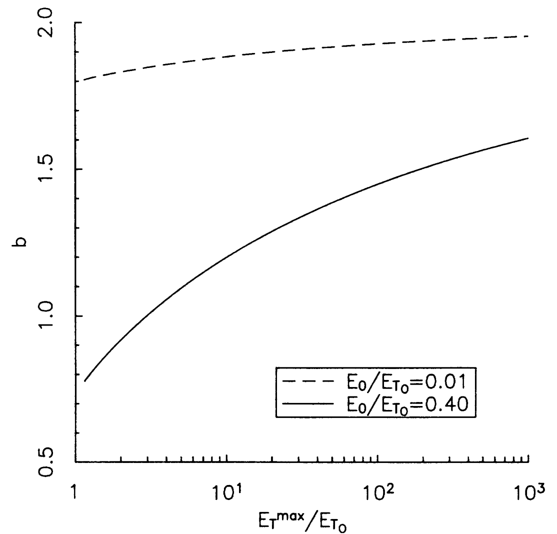


FIG. 26. Power-law exponents obtained from fits of Eq. (10) to the $E_T$-$r_R^{-1}$ relation of Eq. (18) vs the $E$-field range $E_{T_0} < E < E_T^{max}$ over which the fit is performed. The solid and dashed lines indicate exponents expected in the presence of residual pinning for Ti-doped and Ta-doped crystals, respectively. Details of the calculation of the exponent are given in Appendix C.

the CDW. Alternatively, the CDW wave vector might become commensurate with the underlying lattice period near the crystal surface, and thus be strongly pinned.[65]

If surface pinning is important, then some or all of the following features should be expected.

(1) For small crystals, $E_T$ should vary linearly with crystal surface-to-volume ratio, proportional to the circumference to cross-sectional area ratio $C/A$.[13] For ribbonlike $NbSe_3$ crystals with $w \gg t$, $C/A \approx 2/t$, so that $E_T = K/t$.

(2) The constant $K$ in $E_T = K/t$ should depend upon surface preparation conditions but be independent of bulk impurity concentration.

(3) The CDW pinning strength should decay away from the surface over some characteristic length. Consequently, the distribution of pinning strengths within a given crystal should depend upon crystal thickness.

(4) As shown in Sec. V F, an inhomogeneously pinned CDW shears easily when an electric field is applied. Consequently, more weakly pinned regions in the bulk should shear from more strongly pinned regions near the crystal surface, giving rise to a distribution of current densities, broadening of the NBN, rounding of mode-locked Shapiro steps, and an increase in BBN. The magnitude of these effects should depend upon crystal thickness.

Our experimental results provide a detailed test of these expectations for surface pinning. Consistent with feature (1), $E_T$ does vary inversely with crystal thickness in thin crystals. However, contrary to feature (2), the proportionality constant $K$ increases with increasing bulk impurity concentration (Table III) and is approximately proportional to $n_i$. This might result if the pinning strength of the dopant atoms was greatly enhanced near the surface, in which case[66]

$$E_T^{\text{sur}} \approx (Q/e\rho_{\text{eff}})(v\rho_1)^{\text{sur}} n_i^{\text{sur}}(C/A) , \qquad (20)$$

where $n_i^{\text{sur}}$ is the surface impurity concentration. For Ta-doped $NbSe_3$, $n_i^{\text{sur}} \approx (3\times10^{13}\ \text{cm}^{-2})r_R^{-1}$. Using Eq. (20) and the data in Table III gives $(v\rho_1)^{\text{sur}} = 0.5$ meV and 0.3 meV for the $T_{P_1}$ and $T_{P_2}$ CDW's, respectively. These values are much smaller than the bulk pinning strengths $[(v\rho_1)_{\text{Ta}} = 4.3$ and 3.0 meV] calculated in Sec. V B, contrary to the surface-enhanced pinning strength assumption.

An impurity concentration dependence of $K$ might also be expected if commensurability pinning occurs near the crystal surface.[65] Edge dislocations present at boundaries between bulk and surface layers of slightly different CDW wave vector would be charged and thus be pinned by impurities. Since CDW current flow would involve motion of these dislocations, pinning could lead to an $n_i$ dependence of $E_T$ in thin crystals. However, there is no evidence for CDW commensurability near crystal surfaces in $NbSe_3$. Recent small-angle x-ray scattering measurements on $K_{0.3}MoO_3$ found no measurable variation of CDW wave vector with distance from the crystal surface.[67] Similar measurements have not been performed on $NbSe_3$, but there is no reason to expect a different result.

We have also investigated the effect of surface preparation conditions on the size dependence of $E_T$. $NbSe_3$ crystals were exposed to aqua regia vapors for 10 min, resulting in pock marks $\sim$10 $\mu$m apart. These marks had no measurable effect on $E_T$. Crystals were then etched in dilute aqua regia. Long etches roughened the surface and significantly reduced the crystal thickness. However, only the expected $E_T = K/t$ variation with no change in $K$ was observed. These results suggest that surface defects are not responsible for $E_T$'s size dependence.

As stated in feature (3), enhanced CDW pinning near crystal surfaces should result in a thickness-dependent distribution of pinning strengths. This distribution should be reflected in fits to the small-signal ac conductivity in the distribution of crossover frequencies $\omega_{\text{co}}$. The relative magnitudes of the low- and high-frequency components (due to the bulk and surface pinned regions, respectively) and thus the shape of the distribution should vary with thickness. In contrast, although both the characteristic frequency $\omega_{\text{co}}$ and the width of the frequency distribution in the measured ac conductivity vary as $1/t$, the shape of the distribution is independent of $t$. This suggests that the pinning strength distribution is homogeneous within the crystal cross section and varies continuously with thickness. The linear variation of the Shapiro step widths (which reflect the strength of CDW pinning in the sliding state) with $E_T$ and $1/t$ provides additional evidence for this suggestion.

As stated in (4), an inhomogeneously pinned CDW shears easily when an electric field is applied. If the CDW were pinned more strongly near the surface, the bulk CDW would shear from it and begin sliding before the surface CDW depinned. We find no evidence for such shear. First, we have compared the ratios of the low-field single-particle to high-field ($E \approx 20E_T$) CDW conductivities at $T = 50$ K in crystals of different thickness.[68] Since the single-particle conductivity at $T = 50$ K should be essentially independent of thickness, these ratios can be used to estimate the number of layers near the crystal surface where the CDW remains pinned. As shown in Table VIII, the measured ratio for a $t = 0.05$ $\mu$m crystal indicates that the entire cross section depins at high fields, with an uncertainty of $\pm1.5$ unit cell layers.[69] Second, we find no evidence for broadening of the NBN, degradation of mode-locking quality, or increasing

TABLE VIII. Comparison of high-field ($E \sim 20E_T$) and low-field ($E \ll E_T$) conductances $\sigma_H$ and $\sigma_L$ at $T = 50$ K for two crystals of different thickness (Ref. 68).

| $l$ (mm) | $A$ ($\mu$m$^2$) | $t$ ($\mu$m) | $E_T$ (V/cm) | $dV/dI$ (%) ($22.5E/E_T$) | $\sigma_H/\sigma_L - 1$ ($22.5E/E_T$) |
|---|---|---|---|---|---|
| 0.538 | 0.05 | 0.05 | 0.279 | 39.1 | 1.239 |
| 1.11 | 0.67 | 0.35 | 0.0383 | 38.2 | 1.289 |

BBN amplitude with decreasing thickness. In fact, highly coherent NBN, complete mode locking, and low BBN amplitudes are most easily obtained in thinner ($t \leq 2$ $\mu$m) crystals, although this is related to the ease of obtaining crystals with uniform thickness.

In summary, aside from $E_T$'s variation with crystal thickness, we find no evidence for enhanced CDW pinning near crystal surfaces. Surface pinning thus does not provide a viable explanation for the size dependence of CDW properties.

*2. Weak-pinning dimensionality crossover interpretation*

Section VI B showed that 3D weak pinning provides a qualitatively and quantitatively self-consistent account of bulk $E_T$ data for both Ta- and Ti-doped $NbSe_3$. An alternative explanation for the size dependence of $E_T$ follows naturally from weak pinning. In 3D weak pinning, the CDW adjusts its phase in all three spatial directions to optimize its energy of interaction with impurities. From Tables I and VI, the longitudinal ($b$) and transverse ($a^*$) phase-phase correlation lengths for undoped $NbSe_3$ crystals with $r_R \approx 200$ are estimated to be $L_{b^*}^{3D} \approx 20$ $\mu$m and $L_{a^*}^{3D} \approx 2$ $\mu$m, respectively. The latter value is comparable to the thickness of typical crystals. Consequently, in thin crystals such that $t < L_{a^*}^{3D}$, CDW phase variations along $a^*$ should be cut off and a crossover from 3D to 2D weak pinning is expected.

Expressions for the threshold field and phase-phase correlation length in 3D, 2D, and 1D weak pinning were given in Table I. The 2D and 1D expressions must be modified when dimensionality is imposed by a length scale cutoff, i.e., when $L^{3D} > \tilde{t}$ for 2D confinement, or when $L^{3D} > \tilde{t}$ and $\tilde{w}$ for 1D confinement. In 3D, the impurity fluctuation potential per unit volume is $\xi_{imp} \sim v\rho_1 \tilde{n}_i^{1/2}/L^{3/2}$. For the 2D and 1D confinement cases, this becomes $v\rho_1 \tilde{n}_i^{1/2}/(L^2\tilde{t})^{1/2}$ and $v\rho_1 \tilde{n}_i^{1/2}/(L\tilde{t}\tilde{w})^{1/2}$, respectively. In addition, although phase deformations are cut off in the confined directions they remain 3D in character, so that the elastic energies in the 2D and 1D confinement cases are increased by a factor $3/d$ over the strict 2D and 1D cases. The resulting threshold fields and phase-phase correlation lengths for the 2D and 1D confinement cases are summarized in Table IX.[70] In both cases, $E_T$ and the pinning energy per unit volume are increased over their 3D values because confinement reduces the optimum number of impurities in a domain, and thus increases the strength of the fluctuation potential per impurity.

In $NbSe_3$, a crossover to 2D but not 1D pinning is expected because typical crystal widths and lengths are much larger than typical thicknesses, and because CDW correlation lengths (as deduced by x-ray scattering[28,29]) are much longer along $a^*$ than along $c$. Thus, in the weak pinning dimensionality crossover (WPDC) interpretation, the threshold field in thin crystals such that $L_{a^*}^{3D} > t$ is predicted to vary as $E_T^{2D} \propto n_i/t$. Figure 2 showed $E_T$ versus $t^{-1}$ for Ta-doped $NbSe_3$. The solid lines in the thickness-dependent regime represent the fit given by

$$E_T^{(2D)} = (25 \pm 2) r_R^{-1}/t(\mu\text{m}) \ \ \text{V/cm} \ . \tag{21}$$

The quality of this fit is very good. The 2D weak pinning prediction thus qualitatively reproduces both the thickness and impurity concentration dependence of $E_T$ in thin Ta-doped crystals.

The WPDC model also accounts for $E_T$'s size dependence in Ti-doped $NbSe_3$. The ratio

$$(E_T^{(2D)}t)^2/E_T^{(3D)} \approx (\xi_{a^*}/\xi_{b^*})^2(Qf/e\rho_{\text{eff}}) \tag{22}$$

is independent of impurity type and concentration. Consequently, using the ratio $(E_T^{(2D)}t)^2/E_T^{(3D)} = 6.3 \times 10^{-9}$ V cm obtained from the fits of Eqs. (21) and (10) for Ta-doped crystals, $E_T$ in thin Ti-doped $NbSe_3$ crystals can be predicted from $E_T$ in thick crystals with no adjustable parameters. This prediction is indicated by the solid lines in Fig. 7. Although the scatter in the data is considerable, the overall qualitative and quantitative agreement is quite good.

A characteristic thickness $t_c$ for the crossover from 3D to 2D behavior can be obtained from the intersection of the 3D and 2D fits, i.e., from $E_T^{3D} = E_T^{2D}(t = t_c)$. Equating the fits to the bulk and thickness-dependent regimes in Ta-doped crystals given by Eqs. (10) and (21) yields

$$t_c = 0.025 r_R \ \mu\text{m} \ . \tag{23}$$

Theoretically, from Tables I and IX,

$$t_c = 4/3 L_{a^*}^{3D} = (\xi_{a^*}^2 \xi_{c^*}/\xi_{b^*}^3) 45 f^2/(v\rho_1)^2 n_i \ . \tag{24}$$

Substituting for $f$ and $\xi$ from Table VI and using $v\rho_1 = 4.3$ meV yields

$$t_c = 0.0055 r_R \ \mu\text{m} \ . \tag{25}$$

TABLE IX. Weak pinning predictions in 2D and 1D, where dimensionality is imposed by confinement.

| | Phase-phase correlation length ($L$) | Threshold electric field ($E_T$) | Pinning energy per phase coherent domain ($\varepsilon_{dom}$) |
|---|---|---|---|
| $d=2$ | $\dfrac{10\tilde{f}\tilde{t}^{1/2}}{(v\rho_1)\tilde{n}_i^{1/2}}$ | $\dfrac{Q(v\rho_1)^2\tilde{n}_i}{30e\tilde{\rho}_{\text{eff}}\tilde{f}\tilde{t}}$ | $10\tilde{f}\tilde{t}$ |
| $d=1$ | $\dfrac{7.5\tilde{f}^{2/3}(\tilde{t}\tilde{w})^{1/3}}{(v\rho_1)^{2/3}\tilde{n}_i^{1/3}}$ | $\dfrac{Q(v\rho_1)^{4/3}\tilde{n}_i^{2/3}}{9e\tilde{\rho}_{\text{eff}}\tilde{f}^{1/3}(\tilde{t}\tilde{w})^{2/3}}$ | $3(v\rho_1)^{2/3}\tilde{f}^{1/3}\tilde{n}_i^{1/3}(\tilde{t}\tilde{w})^{2/3}$ |

TABLE X. Comparison of the transverse CDW correlation length $L_{a*}$ deduced by x-ray scattering (Ref. 29) with the characteristic thickness $t_c$ for the onset of size dependence of $E_T$ in undoped and Ta-doped $NbSe_3$ at 77 K.

| $r_R$ | $L_{a*}$ ($\mu$m) | $t_c$ ($\mu$m) |
|---|---|---|
| 300 | >1.9 | 5.7 |
| 40 | 0.37 | 0.78 |
| 10 | 0.10 | 0.19 |

The quantitative agreement is reasonable given the crudeness of our theoretical formulas and the uncertainties in our assumed values for the microscopic parameters.

A better comparison is between the crossover thickness $t_c$ and the measured CDW correlation lengths. Sweetland *et al.*[29] have determined the correlation lengths for the $T_{P_1}$ CDW in undoped and Ta-doped $NbSe_3$ by high-resolution x-ray scattering. Table X compares their results for $L_{a*}$ with experimental $t_c$ values given by Eq. (23). Both the magnitudes of the correlation lengths and their dependence on impurity concentration are in excellent agreement with the $t_c$ data. This agreement provides compelling evidence both for weak pinning and for the WPDC interpretation of $E_T$'s size dependence.

The WPDC interpretation is also consistent with the results of ac conductivity, mode locking, and narrow-band noise measurements discussed in Secs. V D–V F. In contrast with surface pinning models, this interpretation predicts that the strength of CDW pinning is homogeneous within the crystal cross section and increases continuously with decreasing thickness. The scaling of the crossover frequency $\omega_{co}$ in the ac conductivity, the low-frequency dielectric constant, and the Shapiro step widths with $E_T$ and thus with thickness, the homogeneous form of the ac response in thin crystals, and the absence of increased CDW shear in thin crystals are all consistent with these predictions.

Thus, the WPDC interpretation provides a qualitatively and quantitatively self-consistent account of the size dependence of $E_T$ and other CDW properties.

### D. Temperature dependence of $E_T$

#### 1. *Increase in $E_T$ as $T \to 0$*

As discussed in Sec. V C, $E_T$ increases with decreasing temperature at temperatures well below $T_P$, where the CDW order parameter is near its $T=0$ value. The most widely cited explanation for this low-temperature increase has been given by Maki and Virosztek.[71] In their model, at finite temperature the local CDW phase fluctuates about its ground-state value $\phi_0$ with amplitude $\langle \delta\phi^2 \rangle \approx 2T/T_0$, where

$$T_0 \approx (2\pi)^2 \tilde{f} \xi_z / k_B \ . \tag{26}$$

These phase fluctuations reduce the effective CDW impurity interaction potential from its $T=0$ value $v\rho_1 \cos[\mathbf{Q}\cdot\mathbf{r}_i + \phi_0(\mathbf{r}_i)]$ by a Debye-Waller factor $e^{-\langle(\delta\phi)^2\rangle/2}$. Assuming $\tilde{f}$ and $\tilde{\rho}_{\rm eff}$ are $T$ independent when $\Delta(T) \approx \Delta(0)$, the usual Lee-Rice arguments then yield

$$E_T(T) \propto e^{-T/T_0'} \ , \tag{27}$$

where $T_0' = mT_0$ and $m=1$, $\frac{1}{4}$, $\frac{1}{2}$, and $\frac{3}{4}$ for strong pinning and 3D, 2D, and 1D weak pinning, respectively. This functional form has been shown to describe $E_T(T)$ in most CDW materials, with the notable exception of $K_{0.3}MoO_3$.[72] As indicated by the dashed lines in Figs. 8–11, it provides a reasonable description of our $E_T(T)$ data as well. However, this model is inconsistent with experiment in several ways.

(i) Substituting parameters appropriate for $NbSe_3$ into Eq. (26) yields $T_0 \approx 500$ K, two orders of magnitude larger than values obtained from fits to the experimental data in Fig. 9.[73]

(ii) The rms CDW phase displacements $\langle(\delta\phi)^2\rangle$ implied by experimental $T_0'$ values are on the order of $\pi$, corresponding to half a CDW wavelength. Such large displacements seem inconsistent with the observed sharp onset of CDW conduction and with memory effects such as the pulse-duration memory effect.[1]

(iii) Experimental $T_0'$ values increase substantially with increasing Ta impurity concentration, as shown in Fig. 10. Brill *et al.*[6] observed a similar increase in Ti-doped samples. $T_0$ in Eq. (26) and thus $T_0'$ are predicted to be independent of impurity concentration and type.

(iv) Experimental $T_0'$ values for the $T_{P_1}$ CDW in the undoped crystals of Fig. 8 do not depend upon crystal thickness. Since the thickest of these crystals is in the 3D weak pinning limit while the thinnest is in the 2D limit, their $T_0'$ values are predicted to vary by a factor of 2.

(v) The CDW phase-phase correlation length $L$ is predicted to vary as $e^{(T/2T_0')}$ and thus to decrease as $T \to 0$. Recent x-ray measurements[29] on Ta-doped $NbSe_3$ show that the CDW correlation length increases continuously from $T_P$ and saturates for $T \ll T_P$.

These many inconsistencies suggest that thermal phase fluctuations are not the cause of $E_T$'s low-temperature increase.

$E_T$'s increase could also arise from a temperature dependence of underlying CDW parameters that is unrelated to the temperature dependence of $\Delta$. Lee and Rice[22] suggested that $E_T$'s increase may be related to a decrease in the effective CDW condensate density $\rho_{\rm eff}$, according to $E_T \propto \rho_{\rm eff}^{-1}$.

As first pointed out by Boriak and Overhauser,[74] the condensate density $\rho_{\rm eff}$, which determines both the CDW electric field coupling ($F_{\rm CDW} = e\rho_{\rm eff}E$) and the current associated with a given CDW velocity ($J_{\rm CDW} = e\rho_{\rm eff}v_D$), differs from the "bare" condensate density $\rho_c$ because of CDW-normal carrier interactions. Using a simple two-fluid model, Lee and Rice[22] showed that

$$\rho_{\rm eff} = \rho_c + \rho_n/(1+\tau/\tau_K) \ , \tag{28}$$

where $\tau_K$ is the normal carrier-lattice relaxation time, $\tau$ is

the normal carrier-CDW relaxation time, and $\rho_c$ and $\rho_n$ are the condensed and normal carrier fractions ($\rho_c+\rho_n=1$). The total force which the CDW feels when an electric field is applied thus consists of the bare force ($\propto \rho_c$) and the force due to normal carrier-CDW interactions [$\propto \rho_n/(1+\tau/\tau_K)$]. Temperature dependence of the coupling parameter $\tau/\tau_K$ will then lead to variations of $\rho_{\text{eff}}$ and $E_T$. For $NbSe_3$, these variations should be largest for the $T_{P_1}$ CDW: Since less than half the room-temperature carrier density condenses into this CDW, $\rho_c$ and $\rho_n$ are comparable so $\tau/\tau_K$ variations could lead to a factor of 2 change in $\rho_{\text{eff}}$.

As discussed in Sec. V C 2, $\rho_{\text{eff}}(T)$ can be deduced from NBN measurements as $\rho_{\text{eff}}=J_{\text{CDW}}/e\lambda\nu_1$, where $\nu_1$ is the fundamental NBN frequency for a current density $J_{\text{CDW}}$. Using this method, Richard and Monceau[75] found that for both CDW's in $NbSe_3$, $\rho_{\text{eff}}$ increased as $T$ decreased from $T_P$ but then decreased again as $T\rightarrow 0$. We have verified their result for the $T_{P_1}$ CDW. Figure 27 shows $\rho_{\text{eff}}$ versus $T$ for two thin $NbSe_3$ samples with high-quality NBN. The maximum value of $\rho_{\text{eff}}$, $2.2\times 10^{21}$ cm$^{-3}$, is close to the value $1.9\times 10^{21}$ cm$^{-3}$ estimated using $\rho_c(T=0)=2/\lambda A_0$ assuming $A_0$ is half the unit-cell area. Below 90 K $\rho_{\text{eff}}$ decreases rapidly, and at 70 K it is roughly half its maximum value.[76]

Figure 28 shows $E_T$ and $1/\rho_{\text{eff}}$ versus $T$. The $E_T$ data are for a thick undoped $NbSe_3$ crystal, and the $1/\rho_{\text{eff}}$ data are for one of the thin crystals in Fig. 27.[77] $1/\rho_{\text{eff}}$ shows the right qualitative behavior. However, the minimum of $E_T$ occurs nearly 30 K higher than that of $1/\rho_{\text{eff}}$, and the overall increase in $E_T$ is larger. A similar but more pronounced discrepancy is observed between $E_T(T)$ and $1/\rho_{\text{eff}}$ data for the $T_{P_2}$ CDW. Thus, the temperature

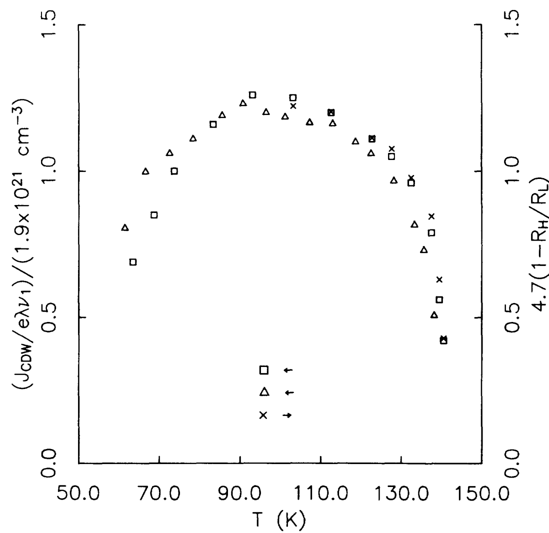


FIG. 27. Effective CDW condensate density $\rho_{\text{eff}}$ vs temperature for the $T_{P_1}$ CDW, as determined from the ratio of the high- and low-field resistances (crosses), and from narrow-band noise measurements on crystals with $t=0.35$ $\mu$m (squares) and $t=0.73$ $\mu$m (triangles).

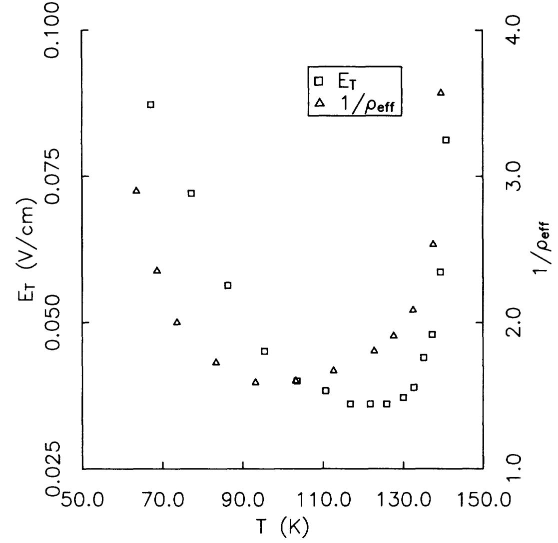


FIG. 28. Threshold electric field $E_T$ and $1/\rho_{\text{eff}}$ vs temperature for the $T_{P_1}$ CDW. The $\rho_{\text{eff}}$ data are for the $t=0.35$ $\mu$m crystal of Fig. 27, while the $E_T$ data are for a crystal with $t=4.7$ $\mu$m.

dependence of $\rho_{\text{eff}}$ provides at best a partial explanation for $E_T$'s low-temperature increase.

### 2. Divergence of $E_T$ as $T\rightarrow T_P$

The divergence of $E_T$ as $T\rightarrow T_P$ is a consequence of the vanishing of the CDW order parameter. In mean-field theory, the effective condensate density varies as[22] $\rho_{\text{eff}}\propto\Delta(T)$ (consistent with the results of Figs. 14 and 27), the CDW phase strain coefficient as[78,79] $f\propto\Delta^2(T)$, and the impurity interaction strength as[22,71,79–82] $v\rho_1\propto\Delta(T)$. Substituting these dependencies into the expressions for $E_T$ of Tables I and IX yields

$$E_T^{\text{weak}}\propto(\rho_{\text{eff}})^{-d/4-d}\ , \tag{29}$$

for weak pinning, and substituting into Eq. (4) yields

$$E_T^{\text{strong}}\propto\text{const} \tag{30}$$

for strong pinning.[83] Thus the exponents $\alpha$ describing $E_T$'s divergence are 1/3, 1 and 3 for 1D, 2D, and 3D weak pinning, respectively, and 0 for strong pinning. Outside the mean-field regime, the same exponents will be obtained as long as $v\rho_1\propto\rho_{\text{eff}}(T)$ and $f\propto\rho_{\text{eff}}^2(T)$.

To compare these predictions with the data of Fig. 15 for the $T_{P_2}$ CDW, we note that $E_T$ remains thickness dependent as $T\rightarrow T_P$ for even the thickest crystals, so that the pinning appears to remain 2D.[84] Assuming that $\rho_{\text{eff}}(T)\approx(1-R_H/R_L)$, for the two thickest crystals ($t=21$ and 4.7 $\mu$m) the measured exponent is $\alpha\approx 0.95\pm 0.05$. This value is consistent with the 2D weak pinning prediction $\alpha=1$. The mean-field analysis thus appears to account for $E_T$'s divergence as $T\rightarrow T_P$ in $NbSe_3$.[85]

### 3. *Threshold rounding in thin crystals near $T_P$*

The rounding of the onset of CDW conduction observed in very thin crystals near $T_P$ in Figs. 16–18 is reminiscent of the rounding of the resistive transition in type-II superconductors, which results from thermally assisted flux flow.[86] The WPDC interpretation suggests that the analogous CDW process—thermally assisted phase flow—may be responsible for the CDW rounding.

For thick undoped $NbSe_3$ crystals, the measured threshold fields and CDW correlation lengths yield pinning energies per phase-coherent domain several orders of magnitude larger than $k_B T$. Consequently, thermal depinning of CDW's should be negligible, consistent with our analysis of the $T \rightarrow 0$ increase of $E_T$. However, in 2D weak pinning, $E_T$ and the pinning energy per unit volume vary as $t^{-1}$ and the phase-coherent domain volume varies as $t^2$. Consequently, the pinning energy per domain $\varepsilon_{\rm dom}$ is reduced from its bulk (3D) $T=0$ value by a factor $[\Delta(T)]^2(t/L_\perp)$, where $L_\perp$ is the bulk $T=0$ transverse phase-phase correlation length. Using an analogy with flux creep in superconductors,[87] the time-averaged CDW drift frequency due to thermal phase "hopping" may be estimated as $\omega_n \sim \omega_p \exp(-\varepsilon_{\rm dom}/k_B T)\sinh(\beta E/k_B T)$, where $\omega_p$ is the pinning frequency and $\beta \sim \varepsilon_{\rm dom}/E_T$. For the $T_{P_2}$ CDW in undoped ($r_R \approx 200$) $NbSe_3$, we estimate $L_{a^*} \approx 4$ $\mu$m and $\varepsilon_{\rm dom}^{3D}(T=0) \approx 3\times10^5$ K. At $T=56$ K, $\Delta(T)/\Delta(0) \approx 0.4$, so that for $t \approx 0.05$ $\mu$m thick crystals, $\varepsilon_{\rm dom}^{2D} \approx 11 k_B T$.[88] This $\varepsilon_{\rm dom}$ is small enough to account for the observed CDW conduction near the nominal $E_T$ in Figs. 16–18. Closer to the Peierls transition $\varepsilon_{\rm dom}$ is even smaller but $E_T$ is increasing, so that interpretation of the detailed form of the *I-V* characteristic is complicated. In sufficiently thin crystals sufficiently near $T_P$, $\varepsilon_{\rm dom}$ becomes so small that the CDW is nearly always depinned and contributes to the $E \rightarrow 0$ conductance, reducing the nonlinear component of the conductance.

Gill[41] has used a similar analysis and reached similar conclusions. He has also proposed an alternative explanation based on the idea that individual edge dislocations control the domain size and thus the pinning energy, but has not attempted to quantify this explanation. Rounding of the onset of CDW conduction might also be expected if phase slip were to occur throughout the crystal volume, allowing independent depinning of regions with different pinning strengths.[89] However, rounding is observed for crystal thicknesses two orders of magnitude larger than the amplitude coherence length ($\xi_{a^*} \approx 10$ Å) and for temperatures where $\Delta(T)$ is a substantial fraction of its $T=0$ value. There is no obvious reason for phase slip to be more prevalent under these conditions.

In summary, the mechanism underlying the $T \rightarrow 0$ increase in $E_T$ is still unclear. However, the divergence of $E_T$ as $T \rightarrow T_{P_2}$ in reasonably thick crystals is well described by 2D weak pinning and mean-field theory. In very thin crystals near $T_{P_2}$, a 2D weak pinning analysis suggests that rounding of the onset of CDW conduction is due to thermally assisted CDW depinning.

## VII. DISCUSSION

### A. Weak versus strong pinning

The character of charge-density-wave pinning in $NbSe_3$ and other CDW conductors has been the subject of controversy for nearly a decade. Weak pinning interpretations were widely used in the early 1980s, but strong pinning interpretations subsequently gained favor. The results of this study allow a thorough evaluation of these interpretations for CDW properties in $NbSe_3$. Our major results and their implications can be summarized as follows.

(i) In thick Ta-doped $NbSe_3$ crystals, $E_T \propto r_R^{-2}$, consistent with 3D weak pinning. In thick Ti-doped crystals, $E_T \propto r_R^{-1.35}$, consistent with a 3D weak pinning analysis, which includes the effects of pinning by residual defects. Both results are inconsistent with strong pinning.

(ii) Weak pinning estimates of impurity interaction strengths $v\rho_1$ from $E_T$-$n_i$ data for Ta- and Ti-doped $NbSe_3$ are consistent with estimates of the pinning parameter $\epsilon_i$. Similar strong pinning estimates are unambiguously inconsistent.

(iii) In thin Ta- and Ti-doped $NbSe_3$ crystals, $E_T \sim (r_R t)^{-1}$; the Shapiro step widths and the crossover frequency of the ac conductivity both scale inversely with crystal thickness $t$; and the pinning within the crystal cross section appears to be homogeneous. These results are consistent with 2D weak pinning. No size dependence of CDW properties is predicted in strong pinning.

(iv) The characteristic crystal thickness $t_c$ for the onset of size-dependent behavior in Ta-doped $NbSe_3$ is comparable to transverse CDW correlation lengths measured by x-ray scattering, consistent with the weak pinning dimensionality crossover interpretation of the size effects. The measured correlation lengths are more than two orders of magnitude larger than the predicted strong pinning correlation length $L \sim n_i^{-1/3}$.

(v) Thickness-dependent rounding of the onset of CDW conduction near $T_P$ is consistent with $t$-dependent energies predicted in 2D weak pinning. No such rounding is predicted in strong pinning.

Together, these results unambiguously rule out conventional strong pinning interpretations, and provide compelling evidence that CDW's in Ta- and Ti-doped $NbSe_3$ are weakly pinned.

### B. Comparison with previous doping studies

As noted in Sec. III, doping studies performed by various authors have yielded strikingly inconsistent results. Our data are generally consistent with those of Brill *et al.*,[6] but are inconsistent with those of most other studies.[7–10] These inconsistencies have resulted because previous studies did not explicitly account for three important factors: (1) the effects of oxygen gettering on dopant concentrations; (2) the effects of pinning by defects other than dopant impurities; and (3) the effects of finite crystal size.

The effects of oxygen gettering on doping studies were mentioned in Sec. IV and are described in detail else-

where.[26] Because of oxygen gettering, impurity concentrations in transported crystals can be much smaller than those in the starting materials, contrary to the usual assumption. Oxygen gettering likely accounts for the more than order-of-magnitude difference between $E_T$ values obtained for comparable Ti-doping levels by Brill *et al.*[6] and by Ido *et al.*[10]

As discussed in Sec. VI B 2, pinning by defects other than dopant atoms has important consequences. Residual defects determine the properties of undoped crystals, which have varied substantially from study to study. For dopants such as Ti, pinning by residual defects can prevent the simple weak and strong pinning power-law dependencies from being expressed except at extremely large doping levels, where $E_T$ may become too large to measure. At smaller doping levels, weak pinning impurities will yield power-law dependencies closer to the simple strong pinning prediction. Like Ti, residual impurities are likely to be charged and affect the $r_R$ more strongly than $E_T$. In Ta-doping studies, residual pinning will thus tend to reduce the $E_T$ values measured for a given $r_R$. This may account for the small $E_T$ values reported for Ta-doped crystals with $r_R \sim 10$ by Underweiser *et al.*[9] and by Monceau.[8]

Inconsistencies have also resulted from finite-size effects. Size effects are significant for both CDW's in $NbSe_3$ in all but the thickest or most heavily doped crystals. They tend to reduce the apparent variation of $E_T$ with impurity concentration (and thus make weakly pinned CDW's appear to be strongly pinned), because the size-related increase in $E_T$ is largest in lightly doped crystals. Size effects also tend to reduce the apparent threshold-field ratio $E_T^{\min}(T_{P_1})/E_T^{\min}(T_{P_2})$. For Ta-doped $NbSe_3$, Underweiser *et al.*[9] obtained a ratio of $\sim 3$. As shown in Fig. 6, we obtain a ratio of $\sim 8$ in thick Ta-doped crystals and a ratio of $\sim 3$ only in rather thin crystals, well into the size-dependent regime. Thus, size effects likely contributed in producing the approximately linear $E_T$-$r_R^{-1}$ relations reported in Ref. 9.

### C. Finite-size effects: Interpretation and implications

The finite-size effects exhibited by CDW's in $NbSe_3$ are truly remarkable. In our highest-purity ($r_R > 300$) crystals, the properties of the $T_{P_2}$ CDW at $T = 50$ K are still strongly thickness dependent in crystals $\sim 50$ $\mu$m thick, the thickest of which we have been able to grow.[90] Such large size effects at such high temperatures are, to our knowledge, unprecedented for transport in a bulk conducting material.

As discussed above, these size effects are qualitatively and quantitatively accounted for by the weak pinning dimensionality crossover interpretation. This interpretation is a very obvious one. In fact, it has long been recognized that CDW properties could become size dependent when crystal dimensions become comparable to CDW correlation lengths. It may then seem peculiar that size effects were not searched for and investigated earlier.

Although many factors have influenced the study and interpretation of size effects,[65,91,92] the TEM measurements of CDW structure in $NbSe_3$ reported by Fung and Steeds[93] and by Chen and Fleming[94] in the early 1980s have undoubtedly been the most important. In dark-field images formed using CDW superlattice reflections, they observed light and dark striations running along the whisker axis with typical lengths (along *b*) of 2 $\mu$m and typical widths (along *c*) of 200 Å. These striations were widely interpreted to be impurity pinned CDW domains. The small transverse dimensions of the striations, at least two orders of magnitude smaller than the dimensions of typical $NbSe_3$ crystals, suggested that size effects produced by a correlation-length confinement mechanism would only be important in extremely tiny crystals.

However, CDW correlation lengths in large undoped $NbSe_3$ crystals cannot be this small. For the $T_{P_2}$ CDW at 50 K, a typical $E_T$ value of $\sim 1$ mV/cm and a domain volume of 2 $\mu$m$\times$200 Å$\times$200 Å would imply a pinning energy per domain of only $\sim 10^{-4}$ eV$\approx 0.25 k_B T$. Such small phase-correlated regions would not be thermally stable and a sharp onset of CDW conduction would not be observed.

The small size of the TEM domains, and the discrepancy between their dimensions and the x-ray determined CDW correlation lengths, have at least a qualitative explanation within the WPDC model. In 2D weak pinning, the CDW correlation lengths in the unconfined directions are reduced from their bulk (3D) values by a factor $(t/L_\perp^{3D})^{1/2}$, where $L_\perp^{3D}$ is the bulk correlation length in the confined direction. The x-ray experiments were performed using thick crystals, and thus measured the bulk correlation lengths. The TEM experiments were performed using extremely thin crystals. For $t \sim 500$ Å typical of TEM samples, the unconfined correlation lengths should be roughly an order of magnitude smaller than their bulk values, and thus roughly comparable with the observed dimensions of the TEM domains.

Size effects provide a natural explanation for large sample-to-sample variations typically observed in CDW properties. Most $NbSe_3$ crystals exhibit complicated NBN spectra, incomplete mode locking, large-amplitude broad-band noise, and a variety of related effects. This complicated, "messy" behavior has been viewed by some[95] to be intrinsic to the CDW response, despite the fact that the detailed behavior varies enormously from crystal to crystal. The present results show that most if not all of this messiness is associated with CDW shear occurring along thickness steps, and that crystal-to-crystal variations are due to variations in crystal cross-sectional shape. Furthermore, they suggest that only crystals with rectangular cross sections (which unfortunately are extremely rare) should be used to characterize intrinsic CDW properties.

The large size of CDW correlation lengths in undoped $NbSe_3$ has important implications for study of CDW dynamics. For example, Fisher[96] has predicted that CDW depinning can be viewed as a dynamical critical phenomenon, exhibiting diverging length and time scales as the threshold $E_T$ is approached from above. In the

critical regime near $E_T$, the dynamical correlation length is predicted to be much larger than the static correlation length. Since typical $NbSe_3$ samples have dimensions of roughly $100\times100\times1$ static correlation lengths, the critical divergence should be cut off and the scaling regime replaced by a finite-size regime. Recent large-scale numerical simulations by Middleton and Fisher[97] and by Myers and Sethna[98] have revealed an interesting finite-size-related structure in the dc $I$-$V$ characteristic above threshold. This structure is large and shows substantial size dependence for numerical "samples" comparable in size to experimental ones. In particular, Myers and Sethna[98] have predicted a sharp dip followed by a "bump" in $dV/dI$ just above threshold which bears a striking resemblance to structure observed in the $dV/dI$'s of extremely high-quality $NbSe_3$ crystals.[99]

Aside from cutting off divergences and modifying distributions near $E_T$, size effects may affect the dimensionality of CDW dynamics. In particular, since the static pinning in most undoped $NbSe_3$ crystals is 2D, the dynamics above threshold may also be 2D. 2D dynamics could account for an apparent discrepancy between the measured form of the high-field CDW $I$-$V$ characteristic and the predictions of the FLR model. Sneddon, Cross, and Fisher[100] and Matsukawa and Takayama[23] have shown that the CDW conductance for $E \gg E_T$ should have the form $\sigma_{\mathrm{CDW}}(E/E_T)=\sigma_b[1-\eta(E/E_T)^{-2+d/2}]$, where $\sigma_b=\sigma_{\mathrm{CDW}}(E\rightarrow\infty)$. For $d=3$, $\sigma_{\mathrm{CDW}}$'s deviation from $\sigma_b$ varies as $1/\sqrt{E}$. However, careful measurements on high-quality $NbSe_3$ crystals[50,99] indicate a $1/E$ deviation, consistent with the prediction for $d=2$. Similarly, experimental data for the ac amplitude dependence of the Shapiro step widths are best fit by predictions for $d=2$.[101] Study of CDW dynamics as a function of crystal size and pinning dimensionality may thus provide new insights and allow more detailed tests of theoretical models than heretofore possible.

### D. Comments on the nature of pinned CDW state

Our finding that Ta, an isoelectronic impurity, pins CDW's in $NbSe_3$ weakly is consistent with most previous expectations. However, our finding that Ti, a charged impurity, also pins weakly with an impurity interaction strength $v\rho_1$ only 2.5 times larger than Ta is surprising. In this final section, we give a more detailed and rather speculative discussion of the implications of these results for the nature of the CDW-impurity interaction in $NbSe_3$.

As noted by Lee and Rice,[22] the Ginzburg-Landau description of the CDW breaks down in the vicinity of an impurity. Using a quantum-mechanical calculation, Tutto and Zawadowski[80] have shown that Friedel oscillations, which have the same $2k_F$ periodicity as the CDW, dominate within roughly an amplitude coherence length of the impurity. The CDW-impurity interaction energy is then determined by the phase mismatch between the tails of the Friedel oscillation and the bulk CDW. The resulting impurity pinning term is similar to that assumed in the FLR model [Eq. (1)] except that (i) $\cos[\mathbf{Q}\cdot\mathbf{r}-\phi(\mathbf{r})]$ is replaced by a periodic function whose shape is determined by the impurity scattering strength; and (ii) screening of the impurity by the Friedel oscillation limits the maximum value of the pinning energy to a few times the CDW gap energy, regardless of the impurity strength.

A very different approach due to Abe[81] and also to Tucker[82] leads to a similar conclusion regarding the maximum impurity pinning energy. Using a phase-only Ginzburg-Landau model, Abe showed that the CDW impurity interaction in 3D is somewhat more complicated than in 1D or 2D. For sufficiently strong impurities, it is energetically favorable in 3D for CDW phase deformations to remain confined within a small region of radius $s$ around each impurity, where $s$ is on the order of an amplitude coherence length. Abe referred to this state as the $S$ state, to distinguish it from the usual weak and strong pinning states discussed by Lee and Rice.[102] For dilute impurity concentrations ($s \ll n_i^{-1/3}$), he examined how short-length-scale deformations in the $S$ state (which we refer to as "dimpling") modify the static effective pinning potential for the far-field phase $\bar{\phi}$. In the weak coupling limit ($v\rho_1 \ll \tilde{f}\xi$), the phase is only slightly deformed near the impurity, and the depth of the effective pinning potential $V(\bar{\phi})$ is roughly equal to the bare pinning strength $v\rho_1$. In the intermediate-to-strong coupling regime ($v\rho_1 \geq \tilde{f}\xi$), the phase is strongly deformed near the impurity. If these deformations become too large, the CDW amplitude collapses, placing an upper limit on the effective pinning strength for an impurity of $(v\rho_1)_{\mathrm{eff}}^{\max}=k\Delta$, where $k$ is a constant of order unity. Tucker[82] has subsequently incorporated Tutto and Zawadowski's microscopic calculation into the Ginzburg-Landau treatment of the $S$ state and has obtained a similar maximum pinning strength.

Thus, the approaches of Tutto and Zawadowski, Abe, and Tucker all predict an impurity interaction strength cutoff of $\sim\Delta$. As a result, differences between the pinning strengths of isoelectronic and charged impurities should be much smaller than the differences between their "bare" impurity potentials. This is qualitatively consistent with the factor of 2.5 difference in pinning strengths we obtained for Ta and Ti. However, the absolute magnitudes we obtained, 4.3 meV for Ta and 11 meV for Ti, are much smaller than the $T_{P_1}$ CDW gap energy deduced from tunneling measurements,[103] listed in Table VI. The calculated value of $v\rho_1$ is sensitive to the microscopic parameter values assumed in Table VI; of these, the value of $f$ is the least certain. In Sec. VI C, we noted that the experimental and theoretical values for the crossover thickness $t_c$ differed by a factor of $\sim5$. Similarly, the experimental and theoretical values for $(E_T^{(2D)}t)^2/E_T^{(3D)}$ differ by $\sim50$. If these discrepancies are entirely attributed to the assumed value of $f$, revised estimates of $(v\rho_1)_{\mathrm{Ta}}\approx80$ meV and $(v\rho_1)_{\mathrm{Ti}}\approx200$ meV are obtained, which are comparable to the CDW gap.[103]

Regardless of the assumed value of $f$, simple estimates (similar to those used by Abe) suggest that $S$-state-type dimpling should occur around both Ta and Ti impurities in $NbSe_3$. Since dimpling is usually associated with strong pinning, how is this consistent with the weak pin-

ning behavior exhibited by both Ta and Ti?

The answer to this apparent contradiction may be related to the ideas of Tucker,[82,104] who examined the $S$ state in detail. He suggested that the macroscopic properties associated with the CDW are determined not by dimpling at individual impurities, but by long-length-scale variations of the phase $\bar{\phi}$ and that the primary effect of dimpling is to yield a modified impurity potential $-\alpha\Delta\cos(\bar{\phi}-\phi_i)$, where $\phi_i$ is the preferred phase at the impurity site and $\alpha$ is a numerical constant of order unity. If these ideas are correct, then the phase-phase correlation lengths and pinning energies should be calculated using the modified impurity potential and the standard energy minimization arguments of Lee and Rice. This implies that the $S$ state reduces to the conventional weak and strong pinning states. Consequently, weak pinning and dimpling can coexist.

This picture of the $S$ state is consistent with Matsukawa's 3D simulations of the FLR model.[23] Matsukawa observed that $E_T \propto \epsilon_i^4$, consistent with the expected weak pinning result, but that the net impurity pinning energy was greater than expected, i.e., $-\mathcal{E}^{\mathrm{imp}}/\mathcal{E}^{\mathrm{el}} > 4/3$. He suggested that this increased pinning energy was due to Abe-type dimpling in the vicinity of the impurities.[105]

This picture of the $S$ state is not consistent with that reached by Tucker.[82,104] Rather than using the Lee-Rice methods for estimating CDW correlation lengths, he assumed the longitudinal correlation length to be the average distance between impurities on a single chain and the transverse correlation length to be the three-dimensional average-impurity spacing. As is discussed in detail elsewhere,[106] these assumed correlation lengths are much smaller than the values measured by x-ray scattering and lead to predictions for CDW properties that are unambiguously inconsistent with experiment. This is not surprising, since these correlations lengths do not reflect the actual anisotropy of CDW materials. The Lee-Rice arguments yield a lower energy and therefore a preferred pinning configuration.

Finally, the above discussion may have important implications for the observability of strong pinning in $NbSe_3$. In 3D, the strong pinning limit may be reached in two ways: by using more strongly perturbing impurities, or by increasing the impurity concentration [cf. Eq. (3)]. However, if the impurity interaction strength is indeed limited by the CDW gap, then it may not be possible to find substitutional impurities significantly more strongly perturbing than Ti. Furthermore, $E_T$ values in the most heavily doped crystals studied here are already near the limits of measurability. Signatures of strong pinning due to more strongly perturbing impurities or to larger impurity concentrations thus might be seen in millimeter wave conductivity measurements or in structural measurements, but may be unobservable in transport properties.

## VIII. CONCLUSION

CDW conductors are among the most remarkable materials ever discovered. The central issue in the study of these materials is the nature of the CDW-impurity interaction. In this paper we have presented a detailed experimental study of the effects of impurity concentration, finite crystal size, and temperature on CDW transport properties. We have shown that CDW's in $NbSe_3$ are weakly pinned by both Ta and Ti impurities, that the characteristic lengths are comparable to typical crystal dimensions, that pinning dimensionality varies with crystal thickness, and that the crystal shape can drastically modify measured CDW properties. By establishing the nature of the pinning and the most important experimental parameters governing the CDW response, the present work provides a solid basis for further understanding of CDW systems. This basis should allow the long-recognized potential of CDW conductors as model systems for many phenomena of interest in condensed-matter physics to be exploited.

## ACKNOWLEDGMENTS

We wish to thank S. Ramakrishna, C. Meyers, J. P. Sethna, A. Middleton, U. Eckern, K. Maki, J. C. Gill, S. V. Zaitsev-Zotov, J. W. Brill, J. Ross, F. Levy, P. Monceau, J. Richard, J. Ditusa, and S. E. Brown for fruitful discussions. R.E.T. is grateful to the late John Bardeen for his support and encouragement during the early stages of this work. Funding was provided by the Alfred P. Sloan Foundation, by the AT&T Foundation, and by NSF Grant No. DMR-89-58515.

## APPENDIX A: ROOM-TEMPERATURE CONDUCTIVITY OF $NbSe_3$

The $b$-axis room-temperature conductivity of $NbSe_3$ was determined as follows. First, extremely large crystals with uniform cross-sectional areas along their length were selected. The length and weight of each crystal was

TABLE XI. Summary of $\sigma_b$ (300 K) data.

| $l$ (cm) | Wt. (g) | Inner contact spacing (cm) | Resistance ($\Omega$) | $\sigma_b$ (300 K) ($\Omega^{-1}\,\mathrm{cm}^{-1}$) |
|---|---|---|---|---|
| 2.53 | $0.547\times10^{-3}$ | 1.63 | 8.829 | $5.46\times10^3$ |
| 3.66 | $0.170\times10^{-3}$ | 1.43 | 36.86 | $5.33\times10^3$ |
| 2.82 | $0.35\times10^{-3}$ | 1.36 | 12.47 | $5.59\times10^3$ |
| 1.96 | $0.175\times10^{-3}$ | 1.10 | 14.82 | $5.30\times10^3$ |
| 2.00 | $0.84\times10^{-3}$ | 1.55 | 4.409 | $5.35\times10^3$ |

measured, and the cross-sectional area calculated from these quantities using the x-ray determined density of 6.39 g/cm. Four-probe conductivity measurements were then used to determine the resistance per unit length $R/l$ and the $b$-axis conductivity calculated using $\sigma = l/RA$. Data for five crystals are summarized in Table XI. The conductivity thus obtained is $\sigma_b(300\ \mathrm{K}) = (5.4 \pm 0.1) \times 10^3\ \Omega^{-1}\,\mathrm{cm}^{-1}$.

## APPENDIX B: ac CONDUCTIVITY FIT

The $\sigma_{\mathrm{CDW}}(\omega)$ data in Figs. 19 and 20 is qualitatively described by the single-coordinate model expressions of Eq. (11). To obtain a more accurate fit a distribution of crossover frequencies $\omega_{\mathrm{co}}$ must be assumed, in order to account for the distribution of pinning strengths experienced by a randomly pinned CDW. We assumed a Lorentzian distribution $D(\omega_{\mathrm{co}}/\Omega) = 1/[(\omega_{\mathrm{co}}/\Omega - 1)^2 + 1]$ and that

$$\mathrm{Im}\sigma(\omega) \propto \int_0^\infty D\left(\frac{\omega_{\mathrm{co}}}{\Omega}\right) \frac{\omega\omega_{\mathrm{co}}}{\omega^2 + \omega_{\mathrm{co}}^2}\, d\omega_{\mathrm{co}} \ . \qquad \text{(B1)}$$

The characteristic frequencies $\Omega$ for the fits in Fig. 20 are 4, 20, and 85 MHz for crystal thicknesses of 3.7, 0.81, and 0.17 $\mu$m, respectively. Other distribution functions (e.g., Gaussian) also yield good fits.

## APPENDIX C: POWER-LAW EXPONENTS WITH RESIDUAL PINNING

Defining $y = E_T/E_0$ and $x = a_w b_i r_R^{-1}/\sqrt{E_0}$, Eq. (18) for the threshold field, which assumes that both the dopants and residual defects pin weakly, becomes

$$y = (1+x)^2 \ . \qquad \text{(C1)}$$

Performing a least-squares fit of $\ln y = a + b \ln x$ to Eq. (C1) over the appropriate range of $x(r_R^{-1})$ gives the apparent power-law exponent $b$. This requires minimizing

$$R = \int [2\ln(1+x) - a - b\ln x]^2 d\ln x \qquad \text{(C2)}$$

with respect to $a$ and $b$, where the limits of the integration are $\ln(\sqrt{E_T^{\max}/E_0} - 1)$ and $\ln(\sqrt{E_{T_0}/E_0} - 1)$ for minimum and maximum threshold fields of $E_{T_0}$ and $E_T^{\max}$. Figure 26 plots $b$ versus $E_T^{\max}/E_{T_0}$ for $E_0/E_{T_0}$ values of 0.4 and 0.01, which correspond to the Ti- and Ta-doping cases, respectively, in Fig. 25.


[1]For comprehensive reviews of CDW's, see *Electronic Properties of Quasi-One-Dimensional Materials*, edited by P. Monceau (Reidel, Dordrecht, 1985), Part II, p. 139; G. Grüner, Rev. Mod. Phys. **60**, 1129 (1988).

[2]P. Monceau, N. P. Ong, A. M. Portis, A. Meerschaut, and J. Rouxel, Phys. Rev. Lett. **37**, 602 (1976).

[3]R. M. Fleming and C. C. Grimes, Phys. Rev. Lett. **42**, 1423 (1979).

[4]G. Gruner, A. Zettl, W. G. Clark, and J. Bardeen, Phys. Rev. B **24**, 7247 (1981).

[5]J. Richard, P. Monceau, and M. Renard, Phys. Rev. B **25**, 948 (1982).

[6]N. P. Ong, J. W. Brill, J. C. Eckert, J. W. Savage, S. K. Khanna, and R. B. Somoano, Phys. Rev. Lett. **42**, 811 (1979); J. W. Brill, N. P. Ong, J. C. Eckert, J. W. Savage, S. K. Khanna, and R. B. Somoano, Phys. Rev. B **23**, 1517 (1981).

[7]P. M. Chaikin, W. W. Fuller, R. Lacoe, J. F. Kwak, R. L. Green, J. C. Eckert, and N. P. Ong, Solid State Commun. **39**, 553 (1981).

[8]P. Monceau, Physica **109-110B**, 1890 (1982).

[9]M. Underweiser, M. Maki, B. Alavi, and G. Gruner, Solid State Commun. **64**, 181 (1987).

[10]M. Ido, Y. Okajima, H. Wakimoto, and M. Oda, Physica **143B**, 54 (1986); M. Ido, Y. Okajima, H. Wakimoto, and M. Oda, J. Phys. Soc. Jpn. **56**, 2503 (1987).

[11]R. V. Coleman, M. P. Everson, H. A. Lu, A. Johnson, and L. M. Falicov, Phys. Rev. B **41**, 460 (1990).

[12]D. V. Borodin, F. Ya. Nad, S. Savitskaja, and S. V. Zaitsev-Zotov, Physica (Amsterdam) **143B**, 73 (1986).

[13]P. J. Yetman and J. C. Gill, Solid State Commun. **62**, 201 (1987).

[14]J. McCarten, M. Maher, T. L. Adelman, and R. E. Thorne, Phys. Rev. Lett. **63**, 2841 (1989).

[15]D. A. DiCarlo, J. McCarten, T. L. Adelman, M. Maher, and R. E. Thorne, Phys. Rev. B **42**, 7643 (1990).

[16]J. McCarten, M. Maher, T. L. Adelman, D. A. DiCarlo, and R. E. Thorne, Phys. Rev. B **43**, 6800 (1991).

[17]M. Maher, T. L. Adelman, J. McCarten, D. A. DiCarlo, and R. E. Thorne, Phys. Rev. B **43**, 9968 (1991).

[18]P. A. Lee, T. M. Rice, and P. W. Anderson, Solid State Commun. **14**, 703 (1974).

[19]H. Frohlich, Proc. R. Soc. London Ser. A **223**, 296 (1954).

[20]H. Fukuyama, J. Phys. Soc. Jpn. **41**, 513 (1976).

[21]H. Fukuyama and P. A. Lee, Phys. Rev. B **17**, 535 (1978).

[22]P. A. Lee and T. M. Rice, Phys. Rev. B **19**, 3970 (1979).

[23]H. Matsukawa and H. Takayama, J. Phys. Soc. Jpn. **56**, 1507 (1987); H. Matsukawa, J. Phys. Soc. Jpn. **56**, 1522 (1987); **57**, 3463 (1988).

[24]Y. Imry and S. Ma, Phys. Rev. Lett. **35**, 1399 (1975).

[25]W. W. Fuller, G. Gruner, P. M. Chaikin, and N. P. Ong, Phys. Rev. B **23**, 6259 (1981).

[26]R. E. Thorne, Phys. Rev. B **45**, 5804 (1992). The crystal-growth methods described in this reference have yielded undoped $NbSe_3$ crystals with $E_T(T = 50\ \mathrm{K}) < 1$ mV/cm and $r_R \sim 400$.

[27]P. Monceau, J. Richard, and M. Renard, Phys. Rev. B **25**, 931 (1982).

[28]A. H. Moudden, J. D. Axe, P. Monceau, and F. Levy, Phys. Rev. Lett. **65**, 223 (1990).

[29]E. Sweetland, C-Y. Tsai, B. A. Winter, J. D. Brock, and R. E. Thorne, Phys. Rev. Lett. **65**, 3168 (1990); J. D. Brock (private communication).

[30]R. M. Fleming, Phys. Rev. B **22**, 5606 (1980).

[31]K. Tsutsumi and T. Tamegai, J. Phys. C **3**, 1677 (1983).

[32]P. Monceau, M. Renard, J. Richard, M. C. Saint-Lager, and Z. Z. Wang, in *Charge Density Waves in Solids*, edited by G. Y. Hutiray and J. Solyom (Springer-Verlag, Berlin, 1985), p. 280.

[33]The onset of switching in the $I$-$V$ characteristic below $T=30$ K complicates interpretation of $E_T(T)$, so data for $T<35$ K are excluded from Fig. 9.
[34]P. M. Horn and D. Guidotti, Phys. Rev. B **16**, 491 (1977).
[35]J. Richard, H. Salva, M. C. Saint-Lager, and P. Monceau, J. Phys. (Paris) **44**, C3-1685 (1983).
[36]Pronounced rounding of the resistive transition in very thin crystals has been reported by D. V. Borodin, S. V. Zaitsev-Zotov, and F. Ya. Nad, Zh. Eksp. Teor. Fiz. **93**, 1394 (1987) [Sov. Phys. JETP **66**, 793 (1987)].
[37]The absolute temperatures for the two crystals in Fig. 13 may differ from those indicated by $\pm 0.25$ K.
[38]K. Maki, Phys. Rev. B **41**, 9308 (1990).
[39]N. P. Ong and P. Monceau, Phys. Rev. B **16**, 3443 (1977).
[40]For the $T_{P_2}$ CDW, the low field resistance anomaly is completely suppressed at high fields, suggesting that the assumption $\mu_L=\mu_H^{\rm CDW}$ is valid.
[41]J. C. Gill, Synth. Met. **43**, 3917 (1991); J. C. Gill and S. V. Zaitsev-Zotov (private communication).
[42]G. Gruner, A. Zawadowski, and P. M. Chaikin, Phys. Rev. Lett. **46**, 511 (1981); P. Monceau, J. Richard, and M. Renard, Phys. Rev. B **25**, 931 (1982); G. Gruner, L. C. Tippie, J. Sanny, W. G. Clark, and N. P. Ong, Phys. Rev. Lett. **45**, 935 (1980).
[43]These expressions are valid for $\omega \ll (\omega_{\rm co}\gamma)^{1/2}$.
[44]Wei-Yu Wu, A. Janossy, and G. Gruner, Solid State Commun. **49**, 1013 (1984).
[45]R. J. Cava, R. M. Fleming, P. Littlewood, E. A. Rietman, L. F. Schneemeyer, and R. G. Dunn, Phys. Rev. B **30**, 3228 (1984); Wei-Yu Wu, L. Mihaly, G. Mozurkewich, and G. Gruner, *ibid.* **33**, 2444 (1986).
[46]Contact resistances were less than 5% of the low-field sample resistance.
[47]For the $t=3.7$ $\mu$m crystal, the crossover frequency is so low that the dielectric constant is evaluated at 0.3 MHz.
[48]P. Monceau, J. Richard, and M. Renard, Phys. Rev. Lett. **45**, 43 (1980).
[49]A. Zettl and G. Gruner, Phys. Rev. B **29**, 775 (1984).
[50]R. E. Thorne, W. G. Lyons, J. W. Lyding, J. R. Tucker, and J. Bardeen, Phys. Rev. B **35**, 6360 (1987); R. E. Thorne, J. S. Hubacek, W. G. Lyons, J. W. Lyding, and J. R. Tucker, *ibid.* **37**, 10 055 (1988).
[51]Ya. Latyshev, V. Minakova, and Yu. A. Rshanov, Pis'ma Zh. Eksp. Teor. Fiz. **46**, 31 (1987) [JETP Lett. **46**, 37 (1987)].
[52]Here nearly complete mode locking means that the increase in $dV/dI$ on the step is at least 90% of the increase required for complete locking.
[53]J. Richard, P. Monceau, M. Papoular, and M. Renard, J. Phys. C **15**, 7157 (1982).
[54]A. Zettl and G. Gruner, Solid State Commun. **46**, 29 (1983).
[55]S. Bhattacharya, J. P. Stokes, M. Robbins, and R. Klemm, Phys. Rev. Lett. **54**, 2453 (1985).
[56]The stresses which produce cracking are likely due to differences between the thermal expansion coefficients of the crystal and of the silver paste contacts.
[57]K. Fuchs, Proc. Cambridge Philos. Soc. **34**, 100 (1938).
[58]E. H. Sondheimer, Adv. Phys. **1**, 1 (1952).
[59]J. C. Hensel, R. T. Tung, J. M. Poate, and F. C. Unterwald, Phys. Rev. Lett. **54**, 1840 (1985).
[60]The effects of surface scattering in an anisotropic material depend upon the nature of the anisotropy. If the Fermi velocity is anisotropic but the relaxation time distribution is isotropic, then Eq. (14) applies with $\kappa=t/l_\perp$, where $l_\perp$ is the mean-free path in the thickness direction (Ref. 58).
[61]N. P. Ong and J. Brill, Phys. Rev. B **18**, 5265 (1978); N. P. Ong, *ibid.* **18**, 5272 (1978).
[62]We have assumed $\Delta(T)=\Delta(0)$ in these calculations.
[63]Both the doped and undoped crystals shown in Fig. 25 were prepared without added oxygen, in order to obtain comparable background impurity concentrations. High-purity undoped crystals ($r_R>250$) were prepared with oxygen to reduce background impurity concentrations.
[64]The large difference in the pinning strengths of Ta and Ti make comparisons at equal concentrations difficult: at concentrations where $E_T$ in Ti-doped crystals is measurable, $E_T$ in Ta-doped crystals is likely determined by other defects because the effects of the Ta impurities are so weak.
[65]J. C. Gill, Europhys. Lett. **11**, 175 (1990).
[66]Equation (21) is obtained from Eq. (4) assuming $\phi_T=1$.
[67]X.-M. Zhu, R. Moret, H. Zabel, I. K. Robinson, E. Vlieg, and R. M. Fleming, Phys. Rev. B **42**, 8791 (1990).
[68]Because the conductivity ratio is a sensitive function of temperature, the data for the two samples quoted in Table VIII were obtained during the same run to minimize sample temperature differences. Measurements on thicker crystals give similar results.
[69]This estimate assumes that all layers in the bulk contribute equally to the high-field conductivity while layers on the surface remain pinned.
[70]For a somewhat different derivation of these equations, see J. Bardeen, Phys. Rev. Lett. **64**, 2297 (1990).
[71]K. Maki, Phys. Rev. B **33**, 2852 (1986); K. Maki and A. Virosztek, *ibid.* **42**, 655 (1990).
[72]C. Schlenker, J. Dumas, C. Escribe-Filippini, and M. Boujida, Phys. Scr. T **29**, 55 (1989).
[73]This discrepancy has been noted by K. Maki (Ref. 71).
[74]M. L. Boriak and A. W. Overhauser, Phys. Rev. B **17**, 2395 (1978).
[75]J. Richard and P. Monceau (private communication).
[76]Below 70 K, broadening of the NBN fundamental increases the uncertainty in estimating $\rho_{\rm eff}$. However, this uncertainty is small compared with the $\rho_{\rm eff}$'s low-temperature decrease.
[77]It is extremely difficult to obtain high-quality NBN in thick crystals because all thick crystals have irregular cross sections.
[78]T. M. Rice, P. A. Lee, and M. C. Cross, Phys. Rev. B **20**, 1345 (1979).
[79]K. Maki and A. Virosztek, Phys. Rev. B **36**, 2910 (1987).
[80]A. Zawadowski and I. Tutto, Synth. Met. **29**, 469 (1989); I. Tutto and A. Zawadowski, Phys. Rev. B **32**, 2449 (1985).
[81]S. Abe, J. Phys. Soc. Jpn. **55**, 1987 (1986).
[82]J. R. Tucker, Phys. Rev. B **40**, 5447 (1989).
[83]Our exponents for the divergence of $E_T$ differ from those of Ref. 79 because we have assumed $\rho_{\rm eff}\propto\Delta$ instead of $\Delta^2$.
[84]This is somewhat surprising since the phase-phase correlation length becomes smaller as $T\rightarrow T_P$, and so a crossover to 3D behavior near $T_P$ is expected.
[85]For a somewhat thinner crystal ($t=1.5$ $\mu$m), $\alpha$ crosses over from $\sim 0.9$ at lower temperatures to $\sim 0.4$ near $T_P$, and for the thinnest crystal ($t=0.29$ $\mu$m), $\alpha=0.44\pm0.04$, fairly close to the 1D weak pinning prediction. However, as suggested in Sec. V C, the 0.45 exponent is likely an artifact of our definition of $E_T$ and of the rounding of the onset of CDW conduction as $T\rightarrow T_P$, which occurs in thin crystals.
[86]For example, see E. H. Brandt, Int. J. Mod. Phys. B **5**, 751 (1991).
[87]P. W. Anderson, Phys. Rev. Lett. **9**, 309 (1962).
[88]The $\varepsilon_{\rm dom}$ estimates are uncertain by an order of magnitude,

due to a factor of ~2 uncertainty in the CDW correlation lengths.

[89]S. N. Coppersmith, Phys. Rev. Lett. **65**, 1044 (1990).

[90]Yetman and Gill (Ref. 13) suggested that size effects were important in all of their crystals, which had an average $r_R$ of 45. However, their analysis was distorted by a spurious data point for a very large crystal, which obscured the finite-size to bulk crossover.

[91]J. R. Tucker, Phys. Rev. Lett. **65**, 270 (1990).

[92]J. C. Gill, Phys. Rev. Lett. **65**, 271 (1990).

[93]K. K. Fung and J. W. Steeds, Phys. Rev. Lett. **45**, 1696 (1980).

[94]C. H. Chen and R. M. Flemming, Solid State Commun. **48**, 777 (1983).

[95]S. Bhattacharya, J. P. Stokes, M. Higgins, and M. Robbins, Phys. Rev. B **40**, 5826 (1989).

[96]D. S. Fisher, Phys. Rev. B **31**, 1396 (1985).

[97]A. A. Middleton and D. S. Fisher (unpublished); A. Middleton, Ph.D. thesis, Princeton University, 1990.

[98]C. Meyers and J. P. Sethna (unpublished); C. Meyers, Ph.D. thesis, Cornell University, 1991.

[99]R. E. Thorne, J. R. Tucker, and John Bardeen, Phys. Rev. Lett. **58**, 828 (1987); R. E. Thorne, Ph.D. thesis, University of Illinois, 1987.

[100]L. Sneddon, M. Cross, and D. Fisher, Phys. Rev. Lett. **49**, 292 (1982).

[101]J. McCarten (unpublished).

[102]Lee and Rice (Ref. 22) recognized that in 3D phase deformations would occur primarily in the immediate vicinity of the impurity, but they did not distinguish the *S* state from normal strong pinning.

[103]A. Fournel, J. P. Sorbier, M. Konczykowski, and P. Monceau, Phys. Rev. Lett. **57**, 2199 (1986); T. Ekino and J. Akimitsu, Jpn. J. Appl. Phys. **26**, 625 (1987).

[104]J. R. Tucker, W. G. Lyons, and G. Gammie, Phys. Rev. B **38**, 1148 (1988).

[105]Matsukawa's simulations used very high impurity concentrations (Ref. 23). Simulations with more dilute concentrations are needed to clarify the significance of the numerical results.

[106]R. E. Thorne and J. McCarten, Phys. Rev. Lett. **65**, 272 (1990); D. A. DiCarlo, J. McCarten, and R. E. Thorne (unpublished).

[107]J. L. Houdeau, M. Marezio, C. Roucau, R. Ayroles, A. Meerschaut, J. Rouxel, and P. Monceau, J. Phys. C **11**, 4117 (1978).

[108]R. M. Fleming, D. E. Moncton, and D. B. McWhan, Phys. Rev. **18**, 5560 (1978).

[109]$\rho_c$ was determined using $\rho_c = 2/(\lambda A_0)$ (Ref. 1).

[110]Since each CDW removes roughly half the Fermi surface, we assume $A_0$ is half the cross sectional area of the unit cell perpendicular to the $b^*$ direction (Refs. 107 and 108).

[111]The Fermi velocity was determined using $v_F = \hbar Q/2m$, where the band mass $m$ is assumed to be the free electron mass.

[112]The anisotropy was determined as the anisotropy of the phase-phase correlation length determined in x-ray measurements (Ref. 29) on the $T_{P_1}$ CDW. The $T_{P_2}$ CDW anisotropy is assumed to be the same as that of the $T_{P_1}$ CDW.